Vol. 92 No. 5 pp. 1753–1768 ACTA GEOLOGICA SINICA (English Edition) Oct. 2018

# Mixing of Enriched Lithospheric Mantle-Derived and Crustal Magmas: Evidence from the Habo Cenozoic Porphyry in Western Yunnan

XIA Bin[1, 2, 3], LU Ye[1, 2, 3], YUAN Yajuan[1, 2, 3, *], CHEN Weiyan[1, 2, 3], ZHANG Xiao[1, 2, 3], XU Chi[1, 2, 3], YU Shengrui[1, 2, 3] and WAN Zhifeng[1, 2, 3]

1 *School of Marine Sciences, Sun Yat-sen University, Guangzhou 510006, China*
2 *Key Laboratory of Offshore Oil Exploration and Development of Guangdong Higher Education Institutes, Guangzhou 51006, China*
3 *Guangdong Provincial Key Laboratory of Marine Resources and Coastal Engineering, Guangzhou 510006, China*

**Abstract: New zircon U–Pb ages, whole-rock geochemistry and zircon Hf isotopes from the Habo porphyry Western Yunnan, China, were determined to provide constraints on the timing of uplift of the Eastern Tibetan Plateau. The intrusive rocks consist of shoshonitic porphyry (syenite porphyry and monzonite porphyry). Zircon laser ablation inductively coupled plasma mass spectrometry (LA-ICP-MS) U–Pb dating indicates coeval emplacement ages of ~35 Ma. The porphyries have alkaline affinities, enrichment in large ion lithophile elements (LILEs) and light rare earth elements (LREEs) (e.g., Rb, Th, U, Pb), with depletion of high field strength elements (HFSEs) (e.g., Nb, Ti, Ta) and weak Eu anomalies. They display uniform Lu–Hf isotopic compositions with negative zircon εHf(t) values ranging from -3.9 to -0.6. The chemical characteristics of the syenite porphyries indicated that they most likely originated from the lower crust, with mantle-derived material involved in their generation. Geochemically, the monzonite porphyries are similar to the syenite porphyries; however, the lower MgO contents suggest that they were produced by different degrees of partial melting of the same lower crust source. Combined with the geochemical and isotopic data in this paper, imply that the alkali-rich porphyries of the Habo polymetallic deposit were derived from the partial melting of lower crust, enriched by mantle magma, formed in a conversion stage from stress extrusion (a strike-slip shear process) to local stress relaxation (a strike-slip pull-apart process) at the Ailaoshao tectonic zone.**

**Key words: geochronology, geochemistry, Lu–Hf isotopes, Habo porphyry, western Yunnan**

## 1 Introduction

The Ailaoshan tectonic belt, bordered on the east by the Yangtze block and the Simao block on the west, is the most important boundary structure on the eastern side of the Sanjiang orogenic belt and has proven useful for the study of the Tethyan evolution. The Ailaoshan tectonic belt produces a banded alkali-rich porphyry of Cenozoic age（e.g., Zhang et al., 1997; Wang et al., 2001; Hou et al., 2003; Wang et al., 2005; Deng et al., 2014; Bui et al., 2016; Yan et al., 2017; Jiang et al., 2018), and many copper-gold-molybdenum deposits with a close genetic relationship to the alkali-rich porphyry. Researchers have studied the genesis mechanism of the alkaline porphyry, with special attention to its relationship to mineralization (e.g., Turner et al., 1996; Chung et al., 1997; Xu et al., 2012; Zhu et al., 2013; Tran and Liu, 2014; Fu et al., 2015; He et al., 2015). The genesis of the Cenozoic alkali-rich porphyry belt is a topic of interest and many scholars continue to study this.

The Habo porphyry Cu–(Mo–Au) deposit, a newly discovered deposit in the southern part of the Jinshajiang-Ailaoshan metallogenic belt, is an economically important component of the alkali-rich porphyry belt in western Yunnan with excellent copper and gold prospecting potential (White et al., 2007). In-depth study on the metallogenic model of this deposit has been conducted by some scholars. Xu et al. (2012) and Yang et al. (2017) reported the molybdenite Re–Os ages of the ore body and

* Corresponding author. E-mail: yuanyaj3@mail.sysu.edu.cn

the age of zircons in the porphyry. However, the petrogenesis of the Habo rock mass remains unclear—especially the geodynamic processes. The porphyry Cu-Au, including Habo deposits, are likely formed by re-melting previously subduction-modified arc lithosphere, triggered by post-subduction lithospheric thickening, lithospheric extension, or mantle lithosphere delamination (Richards, 2009). Based on major- and trace element geochemical characteristics, as well as Sr-Nb isotopes, Zhu et al. (2009, 2013) reported the quartz-monzonite porphyries were derived from the partial melting of a region of thickened lower crust, with assimilated components from a region of phlogopite-bearing lithospheric mantle. In contrast, the Eocene high-K alkaline rocks along the northern Ailaoshan belt may been derived from enriched mantle, possibly with mixing of materials from buried Tethyan oceanic lithosphere and/or crust (Tran et al., 2014). The Habo alkaline porphyry has been studied less than other porphyry in the alkali-rich belt in western Yunnan. To explore the characteristics of the source region and its implication of genetic significance, studies of geochemistry, geochronology (LA-ICP-MS zircon U–Pb dating) and zircon Lu–Hf isotopes of syenite porphyry and monzonite porphyry related to mineralization in the Habo alkali-rich porphyry belt in western Yunnan region are conducted.

## 2 Geological Setting and Sampling

The Sanjiang region hosts a series of thrust-shear belts that formed in response to the Indian–Asian plate collision (Fig. 1a; Metcalfe, 2006, 2013; Hou et al., 2007; Deng et al., 2011, 2012, 2014b; Wang et al., 2014a), including the Ailaoshan shear belt. Extensive strike-slip movement and thrusting along the belt resulted in the formation of the Ailaoshan fault zone (Hou et al., 2007). The fault zone caused lithospheric-scale extension and emplacement of numerous alkali-rich igneous rocks (Zhang et al., 1987;

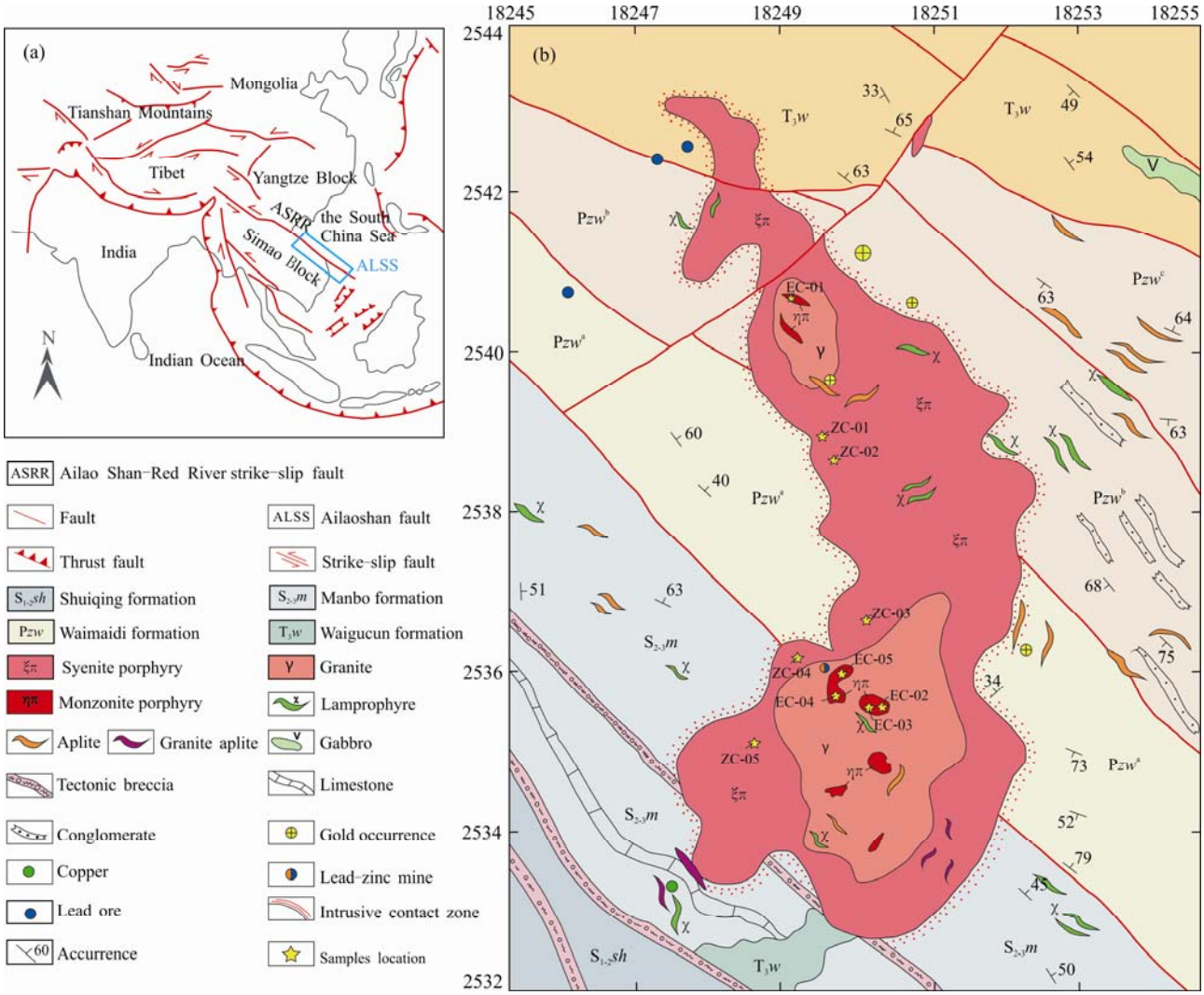


Fig. 1. Tectonic setting (a) and geological map (b) of the Habo mineral district, western Yunnan (modified from Zhu et al., 2013).

Tapponnier et al., 1990; Hou et al., 1996, 2007; Yin and Harrison, 2000). These alkaline igneous rocks vary from basaltic to trachytic and rhyolitic in composition and belong to a group of high-K calc-alkaline and shoshonitic rocks (e.g., Zhang and Xie, 1997；Hou et al., 2003; Bi et al., 2005) with ages varying between 43 and 27 Ma (e.g., Liang et al., 2008; Xu et al., 2012; He et al., 2013, 2016; Zhu et al., 2013; He et al., 2015; Deng et al., 2015; Yang et al., 2017).

The Habo intrusive complex has a surface area of about 12 $km^2$ and is a pluton that outcrops in the southern section of the Ailaoshan fault zone (White et al., 2007), which is also the combination of the western edge of the Yangtze plate and the Lanping-Simao micro-massif. The strata exposed in the study area, ordered from oldest to the youngest, are the Waimaidi lithostratigraphic formation of Paleozoic Madeng lithostratigraphic formation ($P_{zw}$), the Paleozoic Silurian Shuiqing formation ($S_{1\text{-}2sh}$), the Manbo formation ($S_{2\text{-}3m}$) and the Mesozoic upper Triassic Waigucun formation ($T_{3w}$) (Fig. 1b). The Waimaidi lithostratigraphic formation is largely exposed in the middle of the region; the lithology is grayish-yellow metamorphic sandstone, folded gray metamorphic siliceous phyllite, crystalline limestone and gray-black carbonaceous slate. A small area of the Shuiqing formation is exposed in the southwest corner of the region; the lithology exhibits mainly as a gray metamorphic sandstone, metamorphic siltstone and a silty slate. The Manbo formation is exposed in the southern region and the lithology exhibits as gray metamorphic sandstone, metamorphic siltstone, dark gray sericite slate and folded silty slate with a small amount of dark gray crystalline limestone. The Manbo Waimaidi formations have a contact fault relationship. The lithology of the Waigucun formation exhibits as a gray-green metamorphic conglomerate with sandstone and mudstone.

The structure of the study area is mainly characterized by faults with obvious multi-periodicity, divided into the early NW-trending fault zone in the Oumei region and the late NE-trending secondary fault zone in the central region. The granite rock mass in the central part of the area is mainly controlled by NW-trending faults. The main Himalayan magmatic activity in the region, closely related to mineralization, is intense and the intrusive rock is dominated by syenite porphyry, followed by granite, which encroaches on the core of the porphyry body with large intrusions of quartz-monzonite porphyry dykes. A small number of invasive lamprophyre and aplite dykes can also be found in the mass of rock or in the stratum.

Table 1 summarizes the geology and mineralization characteristics of the Habo porphyry. The reserve of the Habo deposit is 20 tons (t) of gold (an average of 5.02 g/t Au) (Mo et al., 1993). K-feldsparization and biotitization occur within quartz–magnetite–pyrite ± chalcopyrite ± molybdenite veins and are the main K-silicate alterations observed in the Habo deposit. The Cu-Au ore body is mainly located outside the K-feldsparization zone, accompanied by medium-intense biotitization, weak K-feldsparation and chloritization. Veins of quartz, quartz–magnetite, quartz–biotite, and sulfides are common. Associated molybdenum ore is produced in a flank of the Cu-Au ore body. The molybdenum-rich ore body mainly occurs on the outer side of the porphyry and develops along the early fault (Zhu et al., 2013). Several deposits (dots), with the main metallogenic species of gold, copper, molybdenum and iron and the main deposit types of porphyry, skarn and epithermal deposits, are found along the early NW-trending regional faults and the NE-trending secondary faults. Laser ablation inductively coupled plasma mass spectrometry (LA-ICP-MS) zircon U–Pb dating yields an age of 36.2±0.2 Ma for the porphyritic granite and Re–Os dating gives an isochron age of 35 Ma for sulfide mineralization (Zhu et al., 2009, 2013).

**Table 1 Characteristics of geology and mineralization of the Habo porphyry (after Mo et al.,1993)**

| | |
|---|---|
| Wall-rock | Triassic sandstone,Siluriansandstone, siltstone, killas |
| Rock type | Syenite porphyry, Monzonitic porphyry, granite, lamprophyre,aplite |
| Alteration | K-silicate alteration,sericitization, carbonatization and skarnization |
| Ore grade | 20t Au, 5.02g/t |
| Orebody shape | lenticular orebodies in the skarn, vein in the porphyry |
| Ore fabric | veins or disseminated veinlet |
| Sulfide association | G+Cp+Py+Bo±Ga±Sp |
| Metallic combination | Au+Cu+Ag±Pb± Zn |

G-native gold, Cp-chalcopyrite, Py-pyrite, Bo- bornite, Ga-galena, Sp-sphalerite

Syenite porphyry dykes are light gray and have hypidiomorphic-allotriomorphic granular texture and a massive structure, with a mineral composition of potash feldspar, plagioclase, hornblende, pyroxene, biotite and other dark-colored minerals. The rocks have weak alteration and fragmentation (Fig. 2a). Monzonite porphyry dykes are dark gray and dark gray-white with a porphyritic, massive structure. The content is 20 to 25% phenocrysts, composed of mainly potassium feldspar and plagioclase. The remaining 75% to 80% is a cryptocrystalline aggregate matrix composed of biotite, plagioclase, amphibolite, and quartz (Fig. 2b).

## 3 Analytical Methods

### 3.1 Whole-rock major and trace elements

The selected whole-rock samples were prepared—first any weathered surfaces were removed, and mostly fresh

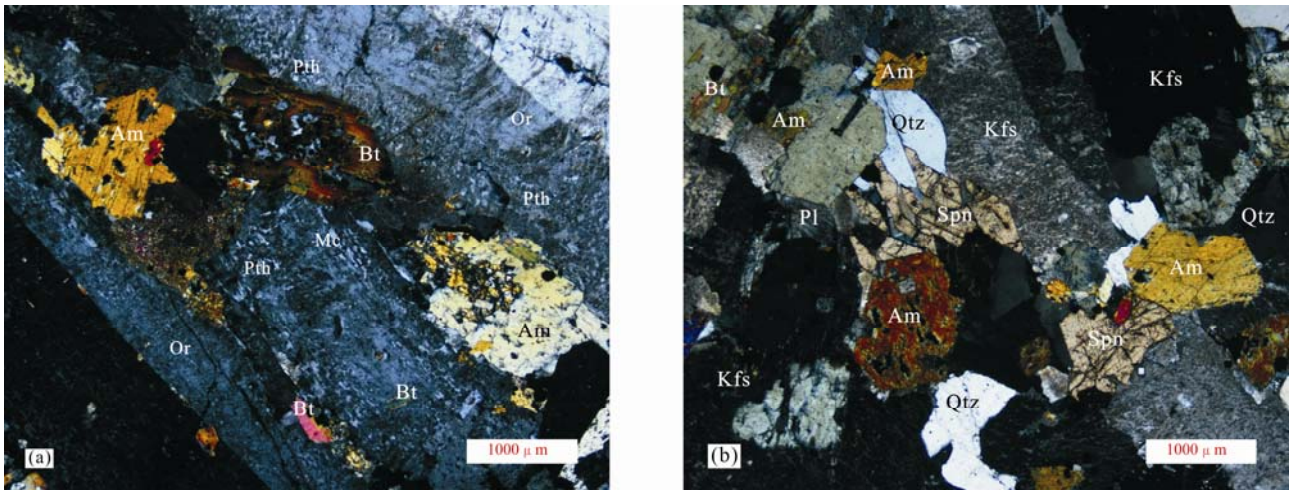


Fig. 2. Photomicrographs of the syenite porphyry and monzonite porphyry from Habo under cross polarized light. (a), syenite porphyry (ZC-02); (b), monzonite porphyry (EC-01). The main mineral of the phenocryst from sample ZC-02 is alkali-feldspar (70-75%), which is mainly orthoclase, perthite and a small amount of microcline. There is intense alteration on the surface of the feldspar, with partially visible carbonatization. The amphibole and biotite contents range from 12 to 15% and 5 to 8%, respectively. The quartz content is low, less than 5%. The phenocryst minerals of from sample EC-01 are K-feldspar (40-45%), quartz (15-18%), amphibole (15-20%), plagioclase (10%), biotite (5%), and sphene (5%). In the figure above, Am-amphibole, Or-orthoclase, Pth-perthite, Bt-biotite, Mc-microcline, Kfs- K-feldspar, Qtz-quartz, Pl-plagioclase, Spn-sphene.

samples were chosen for analysis. The samples were split into small blocks and ultrasonically cleaned in distilled water with 5% $HNO_3$, then, were washed with distilled water. After drying, fresh samples were handpicked. The rocks were crushed and were ground in an agate ring mill, and the resulting powder was used for major and trace element analysis. X-ray fluorescence spectrometry was used to determine the major elements, and a PE Elan 6000 inductively coupled plasma mass spectrometer (ICP-MS) at the Guangzhou Institute of Geochemistry, Chinese Academy of Sciences (GIGCAS), Guangzhou, China was used to measure the trace elements. Analytical uncertainties were ±1–3% for major elements. The uncertainties in the analyses of internal standards and trace elements were ±5% for rare earth elements (REEs) and ±5–10% for trace elements. The analytical procedures used follow those of Chen et al. (2010).

### 3.2 LA-ICP-MS U-Pb zircon geochronology

Laser ablation inductively coupled plasma mass spectrometry (LA-ICP-MS) at the State Key Laboratory of Isotope Geochemistry, Guangzhou Institute of Geochemistry was used to undertake the Zircon U-Pb dating. The internal zircon structure was examined using cathodoluminescence (CL) images prior to U-Pb isotopic analyses. The LA-ICP-MS system used consisted of an Agilent 7500a ICP-MS coupled with a Resonetics RESOlution M-50 ArF excimer laser source (λ=193 nm), using 80 mJ of laser energy, a repetition rate of 10 Hz, a spot diameter of 31 μm, and a 40s ablation time. Helium was used as a carrier gas to carry ablated aerosols to the ICP source (Tu et al. 2011). NIST610 (Pearce et al. 1997) and TEM ($^{206}Pb/^{238}U$=416.8 Ma) were used as external calibration standards (Black et al. 2003), with $^{29}Si$ used as an internal standard. Common Pb was corrected by using observed $^{204}Pb$. Uncertainties of the data points listed in Table 2 are ±1σ.The ages quoted in the text are $^{206}Pb/^{238}U$ (the older age is $^{207}Pb/^{206}Pb$ ages) ages, which were determined by taking the weighted mean at the 95% confidence level. ICP-MS Datacal 7.4 and attached IsoplotI/Ex_ver3 software programs were used for the data processing (Ludwing, 2003; Liu et al., 2008, 2010).

### 3.3 In situ Lu–Hf isotopes

An ArF excimer laser ablation system attached to a Neptune plasma multi-collector ICP-MS at the GIGCAS was used to carry out the analysis of zircon Hf isotope in situ. The instrumental conditions and data acquisition methods were comprehensively described by Woodhead et al. (2004) and Yuan et al. (2004). A stationary spot was used for the present analyses, with a beam diameter of 44 μm, a laser energy density of 80 mJ/pulse, and a repetition rate of 8 Hz, dependent on the size of the ablated domains. Helium was used as the carrier gas to transport the ablated samples from the ablation cell to the ICP-MS torch. To evaluate the quality of the analytical data, a zircon standard (91500) was analyzed. Its $^{176}Hf/^{177}Hf$ ratio was found to be 0.282299 ±31 (2σ), which is consistent with the recommended value.

## 4 Results

### 4.1 Major and trace elements of whole-rock samples

Ten samples were analyzed for major and trace element

**Table 2 Major (wt%), trace element compositions (ppm), and calculated parameters of the Habo porphyry**

| Sample | ZC-01 | ZC-02 | ZC-03 | ZC-04 | ZC-05 | EC-01 | EC-02 | EC-03 | EC-04 | EC-05 |
|---|---|---|---|---|---|---|---|---|---|---|
| Rock type | syenite porphyry | | | | | monzonite porphyry | | | | |
| $SiO_2$ | 59.30 | 63.22 | 63.57 | 59.60 | 59.70 | 68.93 | 68.21 | 68.80 | 69.13 | 69.18 |
| $TiO_2$ | 0.55 | 0.45 | 0.44 | 0.54 | 0.53 | 0.26 | 0.29 | 0.28 | 0.24 | 0.23 |
| $Al_2O_3$ | 13.90 | 14.81 | 15.02 | 14.20 | 14.33 | 14.51 | 14.27 | 14.46 | 14.52 | 14.53 |
| $Fe_2O_{3T}$ | 5.48 | 4.35 | 4.40 | 5.47 | 5.46 | 2.79 | 2.79 | 2.76 | 2.76 | 2.76 |
| MnO | 0.07 | 0.05 | 0.05 | 0.08 | 0.07 | 0.03 | 0.03 | 0.02 | 0.03 | 0.03 |
| MgO | 4.34 | 2.46 | 2.43 | 4.33 | 4.23 | 0.97 | 1.36 | 1.09 | 0.96 | 0.95 |
| CaO | 3.54 | 2.67 | 2.55 | 3.52 | 3.51 | 1.65 | 1.71 | 1.64 | 1.58 | 1.56 |
| $Na_2O$ | 3.44 | 3.48 | 3.48 | 3.45 | 3.47 | 4.22 | 4.04 | 4.22 | 4.08 | 4.11 |
| $K_2O$ | 6.46 | 6.47 | 6.49 | 6.54 | 6.55 | 5.40 | 5.37 | 5.34 | 5.40 | 5.38 |
| $P_2O_5$ | 0.42 | 0.29 | 0.28 | 0.41 | 0.40 | 0.12 | 0.13 | 0.12 | 0.11 | 0.11 |
| LOI | 1.06 | 1.10 | 1.16 | 1.03 | 1.13 | 1.00 | 0.94 | 0.50 | 0.41 | 0.45 |
| Total | 98.56 | 99.35 | 99.87 | 99.17 | 99.38 | 99.88 | 99.14 | 99.23 | 99.22 | 99.29 |
| $Na_2O+K_2O$ | 9.90 | 9.95 | 9.97 | 9.99 | 10.02 | 9.62 | 9.41 | 9.56 | 9.48 | 9.49 |
| $Na_2O/K_2O$ | 0.53 | 0.54 | 0.54 | 0.53 | 0.53 | 0.78 | 0.75 | 0.79 | 0.76 | 0.76 |
| $Mg^{\#}$ | 64.9 | 56.9 | 56.3 | 64.8 | 64.4 | 44.8 | 53.2 | 47.9 | 44.8 | 44.5 |
| Li | 13.6 | 22.1 | 12.9 | 10.2 | 10.1 | 12.8 | 20.2 | 12.7 | 13.1 | 13.0 |
| Be | 14.50 | 18.30 | 12.70 | 12.05 | 12.06 | 11.60 | 13.60 | 11.40 | 9.79 | 9.68 |
| Sc | 12.90 | 10.20 | 7.10 | 12.40 | 12.50 | 5.95 | 4.42 | 3.40 | 4.40 | 4.34 |
| V | 106.0 | 70.5 | 66.0 | 100.0 | 105.0 | 36.7 | 35.8 | 33.0 | 35.0 | 34.0 |
| Cr | 295 | 131 | 130 | 250 | 260 | 58 | 67.5 | 40 | 60 | 59 |
| Co | 18.30 | 11.70 | 10.40 | 16.90 | 17.20 | 5.09 | 5.78 | 4.70 | 5.20 | 5.12 |
| Ni | 108 | 47.2 | 40.1 | 85.8 | 81.8 | 28.4 | 30.0 | 15.0 | 26.4 | 27.4 |
| Cu | 266 | 41.4 | 49.6 | 351.0 | 341.0 | 17.5 | 37.8 | 18.0 | 47.9 | 45.4 |
| Zn | 89.4 | 47.8 | 35.0 | 68.0 | 65.0 | 45.5 | 30.1 | 26.0 | 22.0 | 24.0 |
| Ga | 17.6 | 18.6 | 21.1 | 19.2 | 18.5 | 17.2 | 16.5 | 18.6 | 18.9 | 17.6 |
| Ge | 1.43 | 1.10 | 0.20 | 0.27 | 0.37 | 1.14 | 1.07 | 0.26 | 0.21 | 0.31 |
| As | 9.27 | 9.19 | 8.2 | 9 | 8.8 | 9.7 | 8.94 | 7.7 | 7.4 | 8.2 |
| Rb | 311 | 325 | 321 | 306 | 310 | 282 | 286 | 291 | 285 | 278 |
| Sr | 790 | 845 | 815 | 796 | 790 | 658 | 641 | 675 | 634 | 645 |
| Y | 26.27 | 23.21 | 22.1 | 25.6 | 24.6 | 17.22 | 17.33 | 16.4 | 17.9 | 17.53 |
| Zr | 339 | 316 | 510 | 411 | 401 | 223 | 195 | 228 | 221 | 219 |
| Nb | 15.1 | 18.7 | 18.1 | 16.6 | 15.6 | 13.4 | 12.5 | 14.5 | 12 | 12.5 |
| Sn | 3.96 | 3.56 | 3 | 4 | 3.8 | 2.93 | 3.21 | 3 | 4 | 3.21 |
| Cs | 8.92 | 14.2 | 12.7 | 8.47 | 8.67 | 8.67 | 10.5 | 8.76 | 9.5 | 9.45 |
| Ba | 1410 | 1280 | 1075 | 1330 | 1260 | 870 | 910 | 880 | 834 | 838 |
| Hf | 9.62 | 9.04 | 12.2 | 9.1 | 9.14 | 6.81 | 5.87 | 6.1 | 6.4 | 6.2 |
| Ta | 1.5 | 1.77 | 1.3 | 1.2 | 1.32 | 1.52 | 1.7 | 1.4 | 1.42 | 1.38 |
| Pb | 46 | 42.2 | 34.7 | 42.7 | 43.5 | 44.2 | 40.3 | 52.5 | 34.8 | 34.7 |
| Th | 34.8 | 50.5 | 44.3 | 25.9 | 35.9 | 27.4 | 27.8 | 29.1 | 28.3 | 28.8 |
| U | 11.4 | 13.5 | 11.05 | 9.02 | 10.02 | 14.3 | 14.9 | 12.05 | 12.9 | 12.2 |
| La | 42.4 | 38.5 | 40.7 | 44.3 | 43.8 | 28.3 | 27.8 | 31.6 | 29.8 | 29.6 |
| Ce | 81.1 | 72.9 | 70.2 | 80.9 | 81.4 | 50.3 | 53.3 | 56.9 | 51.0 | 49.0 |
| Pr | 10.1 | 8.58 | 7.99 | 9.91 | 9.83 | 5.51 | 5.96 | 6.07 | 5.59 | 5.62 |
| Nd | 38.3 | 30.8 | 29.3 | 36.2 | 36.8 | 19.0 | 21.2 | 21.1 | 19.7 | 19.6 |
| Sm | 7.45 | 5.97 | 5.56 | 7.63 | 7.53 | 3.70 | 4.18 | 4.05 | 3.73 | 3.65 |
| Eu | 1.75 | 1.51 | 1.3 | 1.57 | 1.49 | 0.76 | 0.9 | 0.81 | 0.8 | 0.79 |
| Gd | 6.85 | 5.58 | 4.95 | 5.94 | 5.9 | 2.68 | 3.82 | 3.25 | 3.15 | 3.08 |
| Tb | 0.99 | 0.75 | 0.64 | 0.85 | 0.86 | 0.48 | 0.55 | 0.51 | 0.49 | 0.47 |
| Dy | 5.18 | 3.65 | 3.43 | 4.66 | 4.65 | 2.62 | 2.93 | 2.78 | 2.76 | 2.74 |
| Ho | 1.03 | 0.77 | 0.56 | 0.91 | 0.91 | 0.58 | 0.64 | 0.58 | 0.54 | 0.57 |
| Er | 2.96 | 2.29 | 2.15 | 2.62 | 2.62 | 1.68 | 1.94 | 1.8 | 1.69 | 1.72 |
| Tm | 0.43 | 0.32 | 0.28 | 0.41 | 0.42 | 0.25 | 0.28 | 0.26 | 0.27 | 0.26 |
| Yb | 3.02 | 2.31 | 1.69 | 2.60 | 2.56 | 1.82 | 2.13 | 1.83 | 1.66 | 1.68 |
| Lu | 0.43 | 0.32 | 0.32 | 0.38 | 0.39 | 0.27 | 0.31 | 0.31 | 0.27 | 0.28 |
| ΣREE | 201.99 | 174.25 | 169.07 | 198.88 | 199.16 | 117.95 | 125.94 | 131.85 | 121.45 | 119.06 |
| ΣLREE | 181.1 | 158.26 | 155.05 | 180.51 | 180.85 | 107.57 | 113.34 | 120.53 | 110.62 | 108.26 |
| ΣHREE | 20.89 | 15.99 | 14.02 | 18.37 | 18.31 | 10.38 | 12.6 | 11.32 | 10.83 | 10.8 |

$Mg^{\#} = 100\times Mg/(Mg^{2+}+Fe^{2+})$

compositions; Table 2 lists the results. According to the Q′-ANOR diagram (Fig. 3a), the Habo syenite porphyry occupies the syenogranite field, whereas the Habo monzonite porphyry falls in the alkali-fsp-Qz granite field. The syenite porphyry has a limited range of $SiO_2$ content (59.30 to 63.57 wt%) while the monzonite porphyry is characterized by slightly higher $SiO_2$ contents (68.21 to 69.18 wt%). Both of the Habo porphyries are shoshonitic and alkaline intrusive rocks with high $K_2O$ contents ($K_2O$=6.46–6.55 wt% for the syenite porphyry, and $K_2O$=5.34–5.40 wt% for the monzonite porphyry) (Fig. 3b–c).

All the samples have $Al_2O_3$ contents ranging from 13.90 to 14.62 wt% and are metaluminous (Fig. 3d), with A/CNK [$Al_2O_3/(CaO+Na_2O+K_2O)$] ranging from 0.75 to 0.94. Harker diagrams for selected major oxides (Fig. 4)

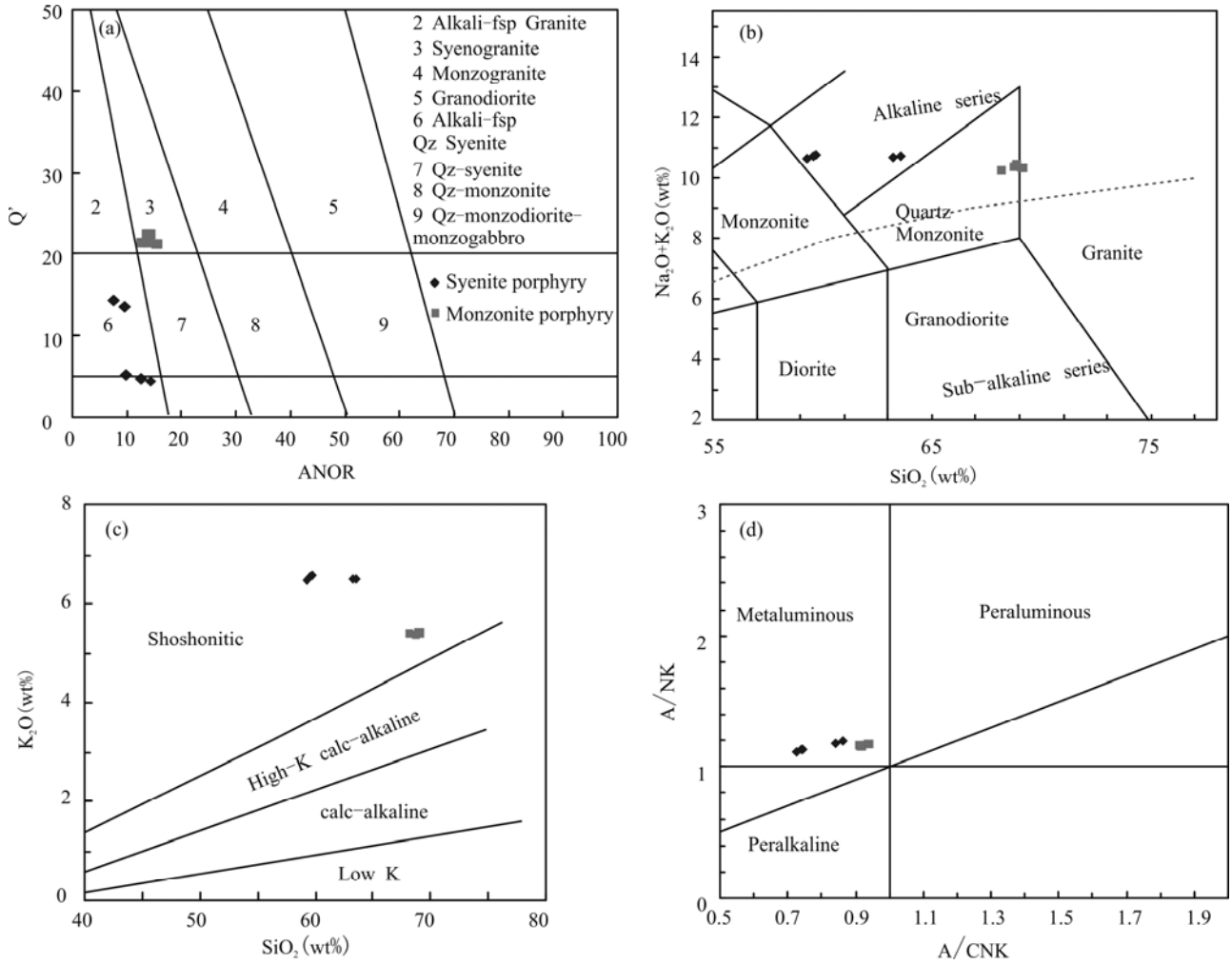


Fig. 3. Chemical classification diagrams for the Habo porphyry.
(a), Q′-ANOR classification diagram (Streckeisen and LeMaitre,1979) for the granitoids, where Q′=100∗Q/(Q+Or+Ab+An) and ANOR=100∗An/(Or+An); (b) Total alkalis ($K_2O$ + $Na_2O$) vs. $SiO_2$ diagram for intrusive rocks (compositional fields from Middlemost, 1994). The boundary line between alkaline and the sub-alkaline series is from Irvine and Baragar (1971); (c), $K_2O$ vs $SiO_2$ diagram (classification boundaries from Rickwood, 1989, and Le Maitre et al., 2002); and (d) A/NK vs. A/CNK diagram (Maniar and Piccoli, 1989), A = $Al_2O_3$, N = $Na_2O$, K = $K_2O$, C = CaO (all in molar proportion).

show that the contents of CaO, $Fe_2O_{3T}$, MgO, $P_2O_5$ and $TiO_2$ correlate negatively with $SiO_2$ contents, and $Al_2O_3$ concentrations correlate positively with $SiO_2$. These results are indicative of fractional crystallization.

The syenite porphyry has a trace element distribution with higher concentrations of Ba, Sr, Nb and Rb than that of the monzonite porphyry (Fig. 5). In the chondrite-normalized REE diagrams, the REE patterns of the porphyry are all characterized by a fractionation between light and heavy REEs. The syenite porphyry contains a total of REE between 169.07 and 201.99 ppm and displays a fractionated REE pattern ($(La/Yb)_N$=10.1–17.3; N denotes chondrite-normalized), with slightly flat heavy REE patterns and negative Eu anomalies with $Eu/Eu^*$ values ranging from 0.68 to 0.80 (Fig. 5). The monzonite porphyry exhibits less total REE than the syenite porphyry does, with total REE ranging from 117.95 to 131.85 ppm, and displays a less fractionated REE pattern ($(La/Yb)_N$=9.4–12.9) with lower $Eu/Eu^*$ values ranging from 0.68 to 0.74 (Fig. 5a). Negative Eu anomalies for all these samples indicate removal of plagioclase by crystal fractionation. Both of the porphyries are enriched in large ion lithophile elements (LILEs) such as Th, U and Rb, and are depleted in high field strength elements (HFSEs), including Ba, Nb, Ta and Ti as the primitive mantle-normalized trace element diagram shows (Fig. 5b).

### 4.2 Geochronology

Table 3 lists the LA-ICP-MS U–Pb zircon data. Zircon grains in samples ZC-02 and EC-01 from the syenite porphyry and monzonite porphyry are mostly euhedral in morphology, transparent, and light yellow in color. Most of them are irregular self-shaped crystals that range in length from 100 to 200 μm. Most of the zircons have oscillatory or planar zoning in CL images (Fig. 6a–b), a typical feature of magmatic zircons (Crofu et al., 2003;

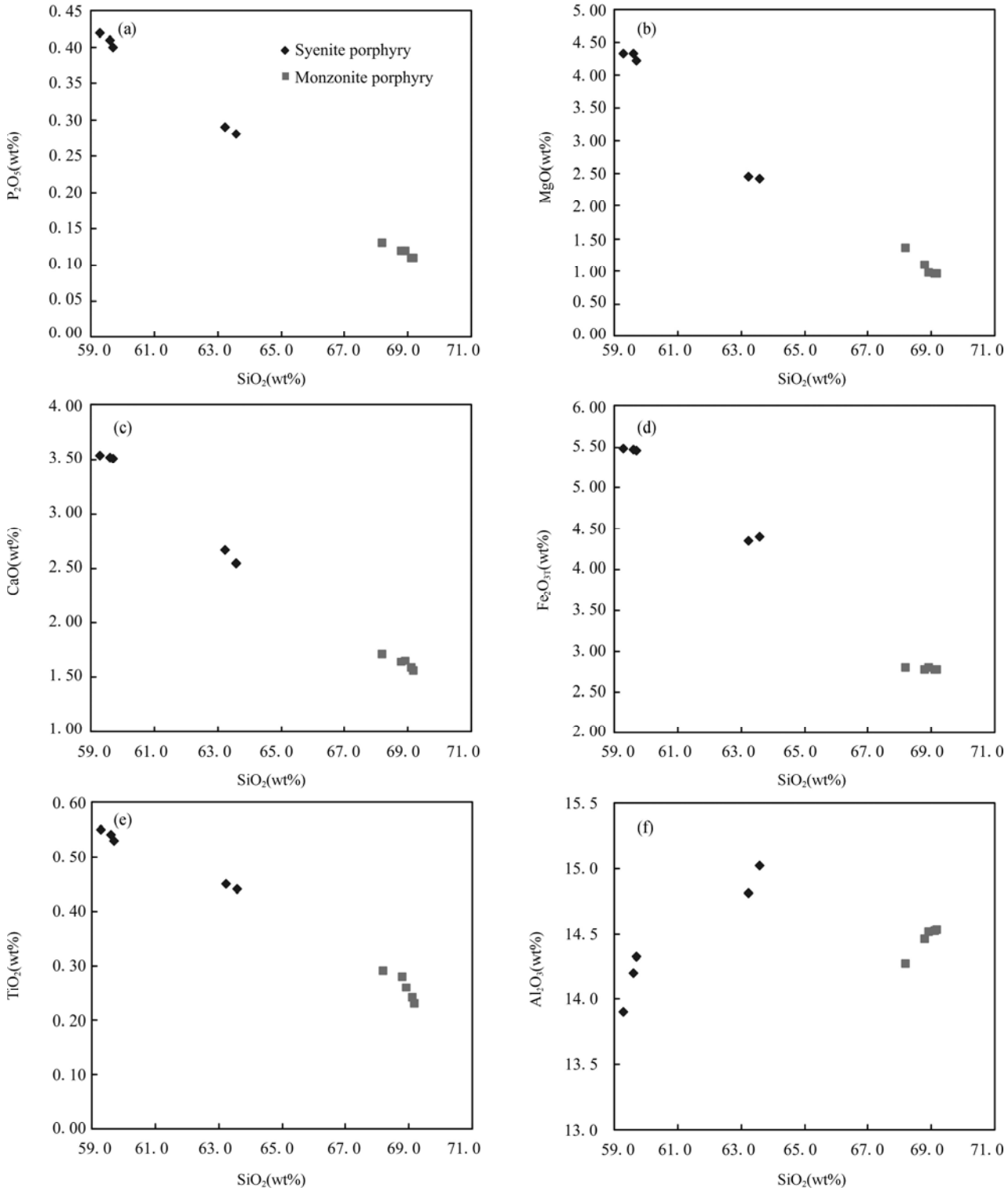


Fig. 4. $SiO_2$ versus oxide diagram of clinopyroxenes.
$Al_2O_3$ contents are positively correlated with $SiO_2$, and with increasing $SiO_2$ contents, CaO, $Fe_2O_{3T}$, MgO, $P_2O_5$, and $TiO_2$ abundances decrease.

Wu and Zheng, 2004).

Thirteen and twelve zircon grains were analyzed for the samples ZC-02 and EC-01 respectively, showing Th/U ratios ranging from 0.37–0.68 and 0.30–0.90, indicating their magmatic origin. The measured $^{206}Pb/^{238}U$ ages are identical within analytical precision, yielding a weighted mean age of 35.25±0.51 Ma (MSWD=2.5) and 34.54±0.63 Ma (MSWD=2.3), respectively (Fig. 6a−b). This is interpreted as the crystallization age of the syenite porphyry and monzonite porphyry.

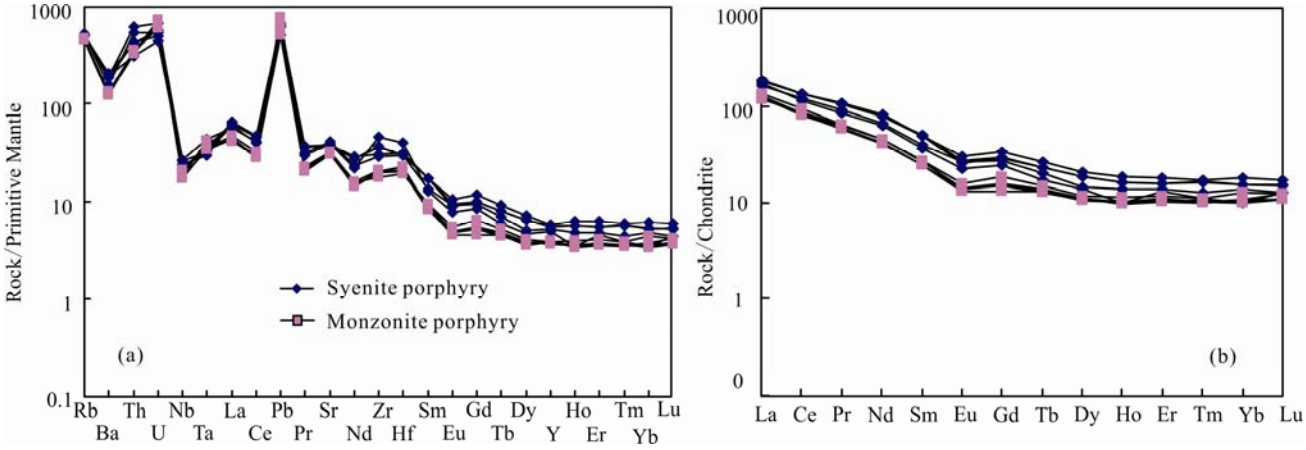


Fig. 5. (a) Primitive mantle-normalized trace element spider patterns and (b) chondrite-normalized REE patterns of the Habo porphyry. Data of primitive mantle and chondrite are from Sun and McDonough (1989).

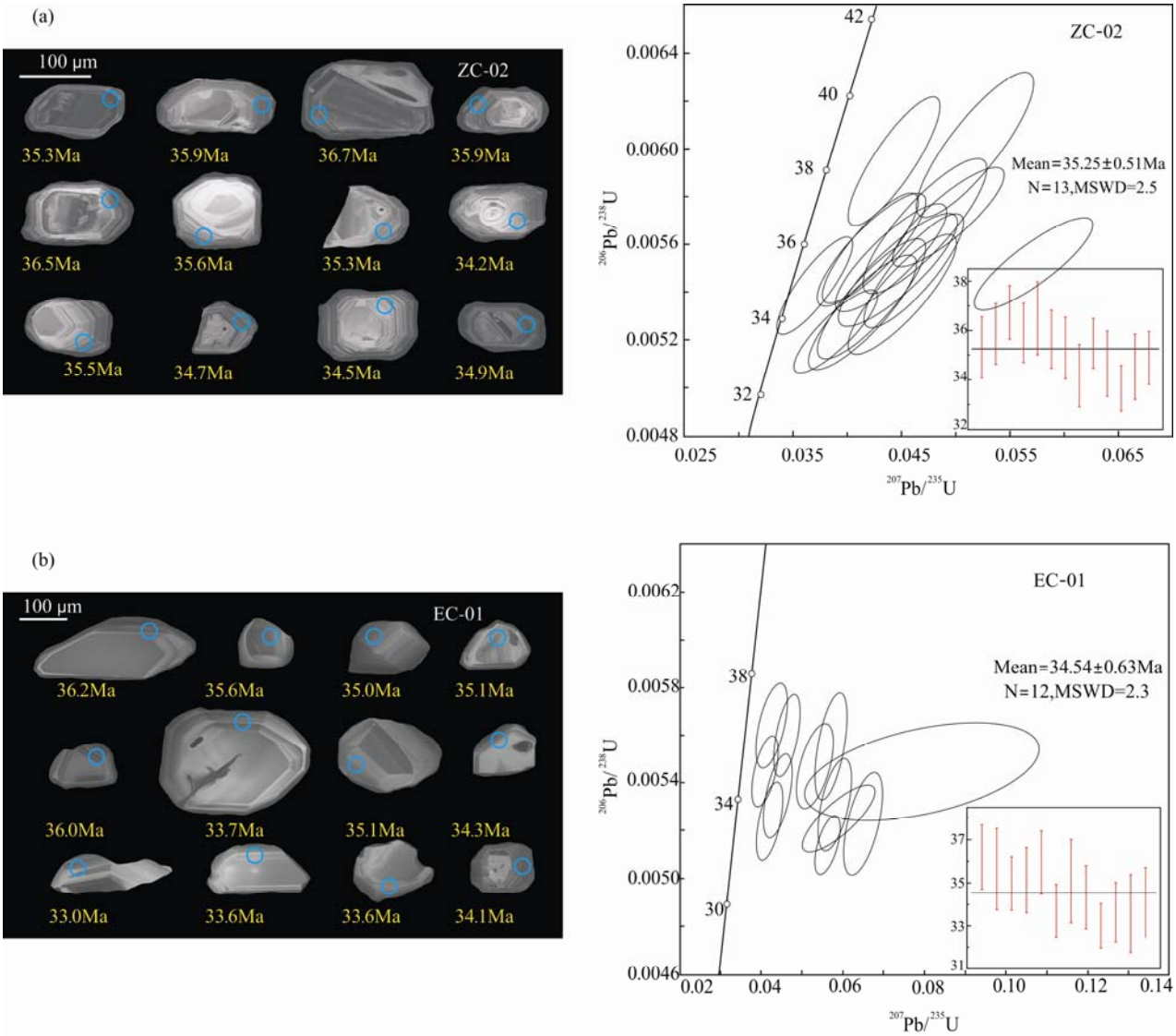


Fig. 6. Cathodoluminescence (CL) image of representative zircons and concordia diagram for zircons from the Habo syenite porphyry (a) and monzonite porphyry (b).

**Table 3 LA-ICP-MS zircon U–Pb analytical results of the samples ZC-02 (syenite porphyry) and EC-01 (monzonite porphyry) from Habo area**

| | Pb | Th | U | Th/U | $^{207}Pb/^{206}Pb$ | 1σ | $^{207}Pb/^{235}U$ | 1σ | $^{206}Pb/^{238}U$ | 1σ | $^{207}Pb/^{235}U$ age (Ma) | 1σ | $^{206}Pb/^{238}U$ age (Ma) | 1σ |
|---|---|---|---|---|---|---|---|---|---|---|---|---|---|---|
| | ppm | | | | | | | | | | | | | |
| ZC-02 (syenite porphyry) | | | | | | | | | | | | | | |
| ZC-02-01 | 6.49 | 406.76 | 1019.35 | 0.40 | 0.06126 | 0.00328 | 0.04467 | 0.00224 | 0.00549 | 0.00010 | 44.4 | 2.2 | 35.3 | 0.6 |
| ZC-02-02 | 7.38 | 742.59 | 1094.24 | 0.68 | 0.05761 | 0.00297 | 0.04223 | 0.00205 | 0.00558 | 0.00010 | 42.0 | 2.0 | 35.9 | 0.6 |
| ZC-02-03 | 7.68 | 565.22 | 1106.35 | 0.51 | 0.06325 | 0.00282 | 0.04932 | 0.00210 | 0.00571 | 0.00008 | 48.9 | 2.0 | 36.7 | 0.5 |
| ZC-02-04 | 7.08 | 584.20 | 1085.83 | 0.54 | 0.05661 | 0.00254 | 0.04213 | 0.00181 | 0.00558 | 0.00009 | 41.9 | 1.8 | 35.9 | 0.6 |
| ZC-02-05 | 5.19 | 419.59 | 805.85 | 0.52 | 0.06523 | 0.00380 | 0.04716 | 0.00233 | 0.00568 | 0.00012 | 46.8 | 2.3 | 36.5 | 0.7 |
| ZC-02-06 | 7.41 | 509.21 | 1192.05 | 0.43 | 0.06034 | 0.00312 | 0.04404 | 0.00210 | 0.00554 | 0.00009 | 43.8 | 2.0 | 35.6 | 0.6 |
| ZC-02-07 | 7.93 | 533.45 | 1288.11 | 0.41 | 0.06383 | 0.00277 | 0.04613 | 0.00187 | 0.00549 | 0.00010 | 45.8 | 1.8 | 35.3 | 0.6 |
| ZC-02-08 | 6.63 | 647.10 | 1056.44 | 0.61 | 0.05801 | 0.00305 | 0.04140 | 0.00204 | 0.00531 | 0.00010 | 41.2 | 2.0 | 34.2 | 0.6 |
| ZC-02-09 | 10.86 | 641.47 | 1648.55 | 0.39 | 0.07612 | 0.00314 | 0.05718 | 0.00223 | 0.00552 | 0.00008 | 56.5 | 2.1 | 35.5 | 0.5 |
| ZC-02-10 | 8.17 | 699.75 | 1278.86 | 0.55 | 0.06606 | 0.00338 | 0.04508 | 0.00204 | 0.00539 | 0.00010 | 44.8 | 2.0 | 34.7 | 0.7 |
| ZC-02-11 | 13.14 | 835.86 | 2245.06 | 0.37 | 0.05447 | 0.00234 | 0.03893 | 0.00158 | 0.00523 | 0.00007 | 38.8 | 1.5 | 33.7 | 0.5 |
| ZC-02-12 | 6.52 | 649.58 | 1031.62 | 0.63 | 0.06125 | 0.00395 | 0.04224 | 0.00204 | 0.00537 | 0.00010 | 42.0 | 2.0 | 34.5 | 0.7 |
| ZC-02-13 | 9.19 | 574.61 | 1546.95 | 0.37 | 0.05090 | 0.00220 | 0.03700 | 0.00143 | 0.00543 | 0.00008 | 36.9 | 1.4 | 34.9 | 0.5 |
| EC-01 (monzonite porphyry) | | | | | | | | | | | | | | |
| EC-01-01 | 4.46 | 554.69 | 614.28 | 0.90 | 0.06181 | 0.00451 | 0.04305 | 0.00246 | 0.00563 | 0.00012 | 42.8 | 2.4 | 36.2 | 0.7 |
| EC-01-02 | 3.71 | 412.77 | 503.72 | 0.82 | 0.08961 | 0.00553 | 0.05754 | 0.00264 | 0.00554 | 0.00015 | 56.8 | 2.5 | 35.6 | 0.9 |
| EC-01-03 | 6.57 | 635.27 | 987.21 | 0.64 | 0.05734 | 0.00308 | 0.04112 | 0.00191 | 0.00544 | 0.00010 | 40.9 | 1.9 | 35.0 | 0.6 |
| EC-01-04 | 3.54 | 304.82 | 536.92 | 0.57 | 0.07433 | 0.00412 | 0.05380 | 0.00291 | 0.00546 | 0.00012 | 53.2 | 2.8 | 35.1 | 0.8 |
| EC-01-05 | 6.84 | 620.73 | 998.95 | 0.62 | 0.06382 | 0.00308 | 0.04697 | 0.00204 | 0.00559 | 0.00011 | 46.6 | 2.0 | 36.0 | 0.7 |
| EC-01-06 | 5.97 | 491.72 | 875.31 | 0.56 | 0.08417 | 0.00901 | 0.05960 | 0.00631 | 0.00524 | 0.00010 | 58.8 | 6.0 | 33.7 | 0.6 |
| EC-01-07 | 2.62 | 249.85 | 382.35 | 0.65 | 0.11480 | 0.01983 | 0.08145 | 0.02010 | 0.00546 | 0.00015 | 79.5 | 18.9 | 35.1 | 1.0 |
| EC-01-08 | 4.31 | 210.27 | 711.11 | 0.30 | 0.06933 | 0.00467 | 0.04456 | 0.00223 | 0.00534 | 0.00011 | 44.3 | 2.2 | 34.3 | 0.7 |
| EC-01-09 | 11.63 | 660.25 | 1735.10 | 0.38 | 0.08249 | 0.00351 | 0.05676 | 0.00214 | 0.00513 | 0.00008 | 56.1 | 2.1 | 33.0 | 0.5 |
| EC-01-10 | 5.42 | 356.64 | 865.42 | 0.41 | 0.06427 | 0.00376 | 0.04246 | 0.00207 | 0.00523 | 0.00011 | 42.2 | 2.0 | 33.6 | 0.7 |
| EC-01-11 | 2.69 | 251.03 | 398.31 | 0.63 | 0.10961 | 0.00892 | 0.06529 | 0.00338 | 0.00522 | 0.00014 | 64.2 | 3.2 | 33.6 | 0.9 |
| EC-01-12 | 3.38 | 260.30 | 506.15 | 0.51 | 0.08973 | 0.00563 | 0.05843 | 0.00287 | 0.00530 | 0.00013 | 57.7 | 2.8 | 34.1 | 0.8 |

### 4.3 Zircon Hf isotopes

In situ zircon Hf isotopic data were analyzed for zircon grains that were previously dated using LA-ICP-MS. Table 4 lists the analytical results and Fig. 7 shows the Hf isotopic evolution diagram. The initial Hf isotopic ratios are recalculated to the crystallization ages.

Eighteen spot analyses on zircons from sample ZC-02 were analyzed for their Hf isotopic composition. $^{176}Hf/^{177}Hf$ ratios range from 0.282651 to 0.282728, and the calculated $\varepsilon Hf(t)$ values vary from −3.5 to −0.8. The corresponding two-stage Hf isotopic crustal model ages ($T_{DM2}$) values range from 1164 to 1339 Ma.

Twenty spot analyses on zircons from sample EC-01 have $^{176}Hf/^{177}Hf$ ratios ranging from 0.282642–0.282733, corresponding to $\varepsilon Hf(t)$ values of −3.9 to −0.6. Two-stage model ages ($T_{DM2}$) are in the range of 728–839 Ma and 1154–1360 Ma.

## 5 Discussion

### 5.1 Ages of porphyry emplacement in Habo deposit

The porphyries from the Habo deposit were all magmatically emplaced over a short period, with ages ranging from 34 Ma to 35 Ma (Table 5, Zhu et al.,2013; Yang et al., 2017; Hu and Huang, 1997; this study), which are coeval with the molybdenite Re–Os ages of 35.47 ± 0.16 Ma (Zhu et al.,2013), implying that the magmatism and mineralization are genetically related. As a whole, the magmatic emplacement ages of the Habo deposit also synchronize well with the potassic and ultrapotassic magmatism along the Jinshajiang-Ailaoshan metallogenic belt (27–43 Ma) (e.g., Chung et al., 1997; Wang et al., 2001; Guo et al., 2005; Liang et al., 2008; Yang et al., 2010; Zhang et al., 2010; Xu et al., 2012; Zhu et al., 2013; He et al., 2013, 2014, 2015, 2016; Deng et al., 2015; Yang et al., 2017). Taking the tectonic context in Jinshajing-Ailaoshan into account, the magmatism is closely related to the transtensional strike-slip movement along the Jinshajiang and Ailaoshan–Red River strike-slip faults that resulted from the Indo-Asian collision (Xu et al., 2012).

### 5.2 Petrogenesis of the porphyries

The aluminum-saturated index (A/CNK) of the Habo porphyries ranges from 0.73 to 0.94, which matches the range of "I" type granite (I-type granite A/CNK < 1.10; Chappell and White, 1992). As $P_2O_5$ content in granite is a more reliable indicator of the genetic type of rock than the aluminum saturation index, $P_2O_5$ and $SiO_2$ in I-type and A-type granites are negatively correlated (Cheng and Mao, 2010; Wang et al., 2015). The $P_2O_5$ content of the Habo porphyries ranges from 0.11 wt% to 0.42 wt% and decreases as $SiO_2$ increases which is also consistent with an I-type granite (Fig. 4a). For further evidence, the Th vs. Rb diagrams (Fig. 8) also show this same trend. Studies indicate that the Th-rich minerals will not crystallize from

**Table 4 Zircon Lu-Hf isotopic data for the samples ZC-02 (syenite porphyry) and EC-01 (monzonite porphyry) from the Habo area**

| | Age (Ma) | $^{176}Yb/^{177}Hf$ | $^{176}Lu/^{177}Hf$ | $^{176}Hf/^{177}Hf$ | 2σ | $^{176}Hf/^{177}Hfi$ | $\varepsilon_{Hf}(0)$ | $\varepsilon_{Hf}(t)$ | $T_{DM}$(Ma) | $T_{DM}^{C}$ (Ma) | $f_{Lu/Hf}$ |
|---|---|---|---|---|---|---|---|---|---|---|---|
| ZC-02 (syenite porphyry) | | | | | | | | | | | |
| ZC-02-01 | 35.25 | 0.018408 | 0.000555 | 0.282677 | 0.000016 | 0.282677 | −3.3 | −2.6 | 805 | 1281 | −0.98 |
| ZC-02-02 | 35.25 | 0.025588 | 0.000784 | 0.282677 | 0.000016 | 0.282676 | −3.4 | −2.6 | 811 | 1283 | −0.98 |
| ZC-02-03 | 35.25 | 0.018430 | 0.000697 | 0.282721 | 0.000016 | 0.282721 | −1.8 | −1.0 | 746 | 1181 | −0.98 |
| ZC-02-04 | 35.25 | 0.023262 | 0.000560 | 0.282707 | 0.000016 | 0.282706 | −2.3 | −1.5 | 764 | 1214 | −0.98 |
| ZC-02-05 | 35.25 | 0.015340 | 0.000478 | 0.282698 | 0.000016 | 0.282698 | −2.6 | −1.8 | 775 | 1233 | −0.99 |
| ZC-02-06 | 35.25 | 0.032681 | 0.000997 | 0.282651 | 0.000017 | 0.282650 | −4.3 | −3.5 | 853 | 1342 | −0.97 |
| ZC-02-07 | 35.25 | 0.020426 | 0.000643 | 0.282697 | 0.000017 | 0.282696 | −2.7 | −1.9 | 780 | 1237 | −0.98 |
| ZC-02-08 | 35.25 | 0.019495 | 0.000621 | 0.282686 | 0.000026 | 0.282685 | −3.0 | −2.3 | 795 | 1261 | −0.98 |
| ZC-02-09 | 35.25 | 0.018798 | 0.000614 | 0.282715 | 0.000015 | 0.282715 | −2.0 | −1.3 | 754 | 1195 | −0.98 |
| ZC-02-10 | 35.25 | 0.010043 | 0.000308 | 0.282657 | 0.000016 | 0.282657 | −4.1 | −3.3 | 828 | 1326 | −0.99 |
| ZC-02-11 | 35.25 | 0.021094 | 0.000662 | 0.282728 | 0.000016 | 0.282728 | −1.6 | −0.8 | 736 | 1166 | −0.98 |
| ZC-02-12 | 35.25 | 0.015336 | 0.000497 | 0.282678 | 0.000018 | 0.282678 | −3.3 | −2.6 | 803 | 1279 | −0.99 |
| ZC-02-13 | 35.25 | 0.015725 | 0.000467 | 0.282707 | 0.000015 | 0.282707 | −2.3 | −1.5 | 762 | 1214 | −0.99 |
| ZC-02-14 | 35.25 | 0.016977 | 0.000529 | 0.282724 | 0.000015 | 0.282724 | −1.7 | −0.9 | 739 | 1174 | −0.98 |
| ZC-02-15 | 35.25 | 0.022682 | 0.000693 | 0.282701 | 0.000013 | 0.282701 | −2.5 | −1.7 | 775 | 1227 | −0.98 |
| ZC-02-16 | 35.25 | 0.015886 | 0.000509 | 0.282674 | 0.000016 | 0.282673 | −3.5 | −2.7 | 809 | 1289 | −0.98 |
| ZC-02-17 | 35.25 | 0.016674 | 0.000520 | 0.282690 | 0.000019 | 0.282690 | −2.9 | −2.1 | 786 | 1251 | −0.98 |
| ZC-02-18 | 35.25 | 0.027497 | 0.000809 | 0.282664 | 0.000016 | 0.282664 | −3.8 | −3.1 | 829 | 1311 | −0.98 |
| EC-01 (monzonite porphyry) | | | | | | | | | | | |
| EC-01-01 | 34.54 | 0.028482 | 0.000939 | 0.282733 | 0.000016 | 0.282733 | −1.4 | −0.6 | 735 | 1156 | −0.97 |
| EC-01-02 | 34.54 | 0.027556 | 0.000846 | 0.282705 | 0.000012 | 0.282705 | −2.4 | −1.6 | 772 | 1218 | −0.97 |
| EC-01-03 | 34.54 | 0.026229 | 0.000835 | 0.282732 | 0.000013 | 0.282731 | −1.4 | −0.7 | 734 | 1158 | −0.97 |
| EC-01-04 | 34.54 | 0.025066 | 0.000738 | 0.282700 | 0.000015 | 0.282700 | −2.5 | −1.8 | 777 | 1230 | −0.98 |
| EC-01-05 | 34.54 | 0.028541 | 0.000868 | 0.282664 | 0.000014 | 0.282663 | −3.8 | −3.1 | 831 | 1312 | −0.97 |
| EC-01-06 | 34.54 | 0.021504 | 0.000623 | 0.282726 | 0.000015 | 0.282726 | −1.6 | −0.9 | 738 | 1170 | −0.98 |
| EC-01-07 | 34.54 | 0.023210 | 0.000695 | 0.282651 | 0.000017 | 0.282651 | −4.3 | −3.5 | 845 | 1340 | −0.98 |
| EC-01-08 | 34.54 | 0.022221 | 0.000708 | 0.282665 | 0.000017 | 0.282665 | −3.8 | −3.0 | 825 | 1308 | −0.98 |
| EC-01-09 | 34.54 | 0.023255 | 0.000775 | 0.282721 | 0.000014 | 0.282720 | −1.8 | −1.1 | 749 | 1183 | −0.98 |
| EC-01-10 | 34.54 | 0.024108 | 0.000762 | 0.282695 | 0.000014 | 0.282694 | −2.7 | −2.0 | 785 | 1242 | −0.98 |
| EC-01-11 | 34.54 | 0.021102 | 0.000641 | 0.282670 | 0.000016 | 0.282670 | −3.6 | −2.9 | 817 | 1297 | −0.98 |
| EC-01-12 | 34.54 | 0.039609 | 0.001224 | 0.282642 | 0.000019 | 0.282641 | −4.6 | −3.9 | 870 | 1362 | −0.96 |
| EC-01-13 | 34.54 | 0.028103 | 0.000861 | 0.282720 | 0.000016 | 0.282720 | −1.8 | −1.1 | 751 | 1185 | −0.97 |
| EC-01-14 | 34.54 | 0.026994 | 0.000846 | 0.282674 | 0.000017 | 0.282673 | −3.5 | −2.7 | 817 | 1290 | −0.97 |
| EC-01-15 | 34.54 | 0.028445 | 0.000912 | 0.282701 | 0.000017 | 0.282701 | −2.5 | −1.8 | 779 | 1227 | −0.97 |
| EC-01-16 | 34.54 | 0.018087 | 0.000571 | 0.282716 | 0.000014 | 0.282716 | −2.0 | −1.2 | 751 | 1194 | −0.98 |
| EC-01-17 | 34.54 | 0.035087 | 0.001070 | 0.282702 | 0.000014 | 0.282701 | −2.5 | −1.8 | 782 | 1227 | −0.97 |
| EC-01-18 | 34.54 | 0.033863 | 0.001032 | 0.282731 | 0.000014 | 0.282730 | −1.5 | −0.7 | 740 | 1161 | −0.97 |
| EC-01-19 | 34.54 | 0.027549 | 0.000851 | 0.282712 | 0.000015 | 0.282711 | −2.1 | −1.4 | 763 | 1203 | −0.97 |
| EC-01-20 | 34.54 | 0.028841 | 0.000835 | 0.282671 | 0.000016 | 0.282670 | −3.6 | −2.8 | 820 | 1296 | −0.97 |

**Table 5 The published data of diagenetic and mineralization ages from the Habo mining area**

| Rock type | sample | Method | Age (Ma) | reference |
|---|---|---|---|---|
| Syenite porphyry | Zircon | LA-ICP-MS U-Pb | 36.2±0.2 | Zhu et al. (2009) |
| Quartz monzonite porphyry | Zircon | LA-ICP-MS U-Pb | 36.19±0.22 | Zhu et al. (2009) |
| Granite | Zircon | LA-ICP-MS U-Pb | 35.4±0.5 | Zhu et al. (2013) |
| Sulfides quartz veinlets | Molybdenite | Re – Os | 35.47±0.16 | Zhu et al. (2009) |
| Quartz syenite | Whole rock | Rb – Sr | 37.50 | Luo et al. (1998) |
| Syenite porphyry | Whole rock | Rb – Sr | 37.30 | Hu and Huang (1997) |
| Quartz syenite | Whole rock + minerals | Rb – Sr | 37.30 | Hu and Huang (1997) |
| Quartz syenite | Whole rock + minerals | Rb – Sr | 37.50 | Hu and Huang (1997) |
| Monzonite porphyry | Whole rock | Rb – Sr | 37.30 | BGMRYP (1990) |
| Syenite porphyry | Zircon | LA-ICP-MS U-Pb | 35.25±0.51 | This study |
| Monzonite porphyry | Zircon | LA-ICP-MS U-Pb | 34.54±0.63 | This study |

BGMRYP: Bureau of Geology and Mineral Resources of Yunnan Province.

a metaluminous I-type granite during the early stages of magmatic differentiation, consequently resulting in high Th abundances and a positive correlation between Th and Rb in differentiated I-type granites (Zhu et al., 2009). The above interpretations suggest that the Habo porphyries are I-type granite.

These porphyries have uniform Sr–Nd isotopic compositions ($\varepsilon$Nd($t$)=−5.3 to −3.7) (Zhu et al., 2013) distinct from the asthenosphere-derived Miocene Maguan Lava ($\varepsilon$Nd($t$)=5 to 7; Xia and Xu, 2004) in Yunnan, which indicate that the syenite porphyries and monzonite porphyries were not derived from the asthenosphere. Combined with their similar enriched zircon Lu–Hf isotopic ratios ($\varepsilon$Hf($t$) =−3.9 to −0.6), this suggest that they originated from the same enriched mantle source, consistent with their high concentrations of REE, especially LREE and LILEs.

The syenite porphyries have relatively high $Mg^{\#}$ (56.3

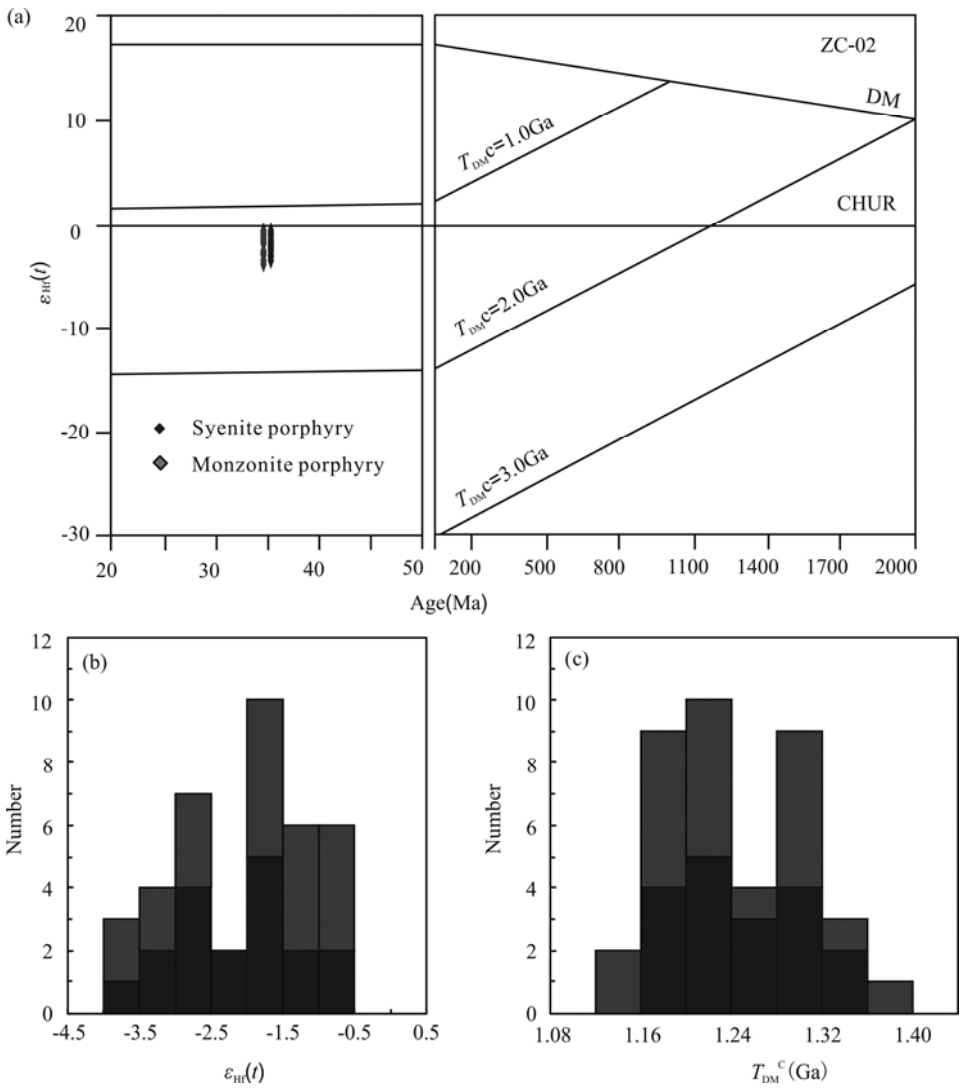


Fig. 7. (a), $\varepsilon_{Hf}(t)$ vs. U–Pb age diagram; (b), histograms of zircon $\varepsilon_{Hf}(t)$ values; (c), histograms of zircon Hf isotope crust model age ($T_{DM}^{C}$).

to 64.8), showing the characteristics of near-primary melts. Their similar MgO, $Fe_2O_{3T}$, $TiO_2$, CaO, Cr, and Ni concentrations are consistent with the lower-middle crustal amphibolite xenoliths hosted by the Eocene potassic felsic intrusions in western Yunnan (Deng et al., 1998), indicating that they may form by partial melting of a mafic crustal source. Furthermore, the weak negative Eu anomalies (*Eu/Eu=0.68–0.80) suggest that the syenite porphyries were derived from a thickened lower crust (Deng et al., 1998). The negative zircon $\varepsilon$Hf($t$) values suggest an ancient metasedimentary rock component (Fig. 7). However, these granite porphyries have a high Th/Yb ratio (10 to 21) and Yb/Hf ratio (<1.2), of which the absolute values are far lower than in crust-derived magmatic rocks (Yogodzinski et al, 2010). These values could be explained if mantle-derived material was involved (Barry et al., 2006; Bolhar et al., 2008). Consequently, these lines of evidence demonstrate that the

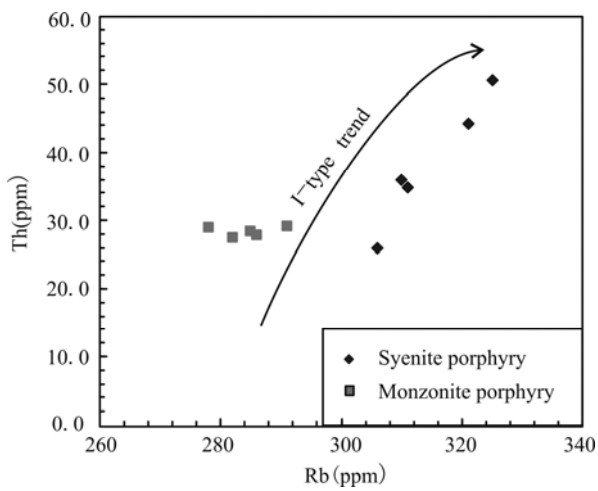


Fig. 8. Th vs. Rb diagram for granitoid classification for samples from the Habo porphyries.

Habo syenite porphyries most likely originated from the lower crust, with the involvement of mantle-derived

material in petrogenesis (e.g., Lu et al., 2012; Liu et al., 2015). The data plot along a partial melting trend line in the La/Sm vs. La and La/Yb vs. La diagrams (Fig. 9a–b), indicating that partial melting of the source, rather than fractional crystallization, was the dominant process. According to melting experiments of phlogopite-bearing mantle at 1 GPa, primary silica-rich potassic magmas can be produced directly by the melting of metasomatized, phlogopite-bearing peridotite (Condamine and Médard, 2014), which is consistent with the origin proposed here for the syenite porphyries. However, weak negative correlations of $TiO_2$, $Fe_2O_{3T}$, MgO, and CaO with $SiO_2$ for these syenite porphyries imply some fractionation of olivine and/or clinopyroxene prior to the emplacement of the magmas (Fig. 4).

The monzonite porphyries were intruded into the syenite porphyries and show a close spatial relationship with them (Fig. 1b), sharing the same shoshonitic and alkaline characteristics, with similar A/CNK ratios (0.92–0.94) (Fig. 3d). They both follow the partial melting trend in the La/Sm vs. Sm and La/Yb vs. La diagrams (Fig. 9a–b). The MgO contents of the monzonite porphyries are lower than the syenite porphyries (Table 1) suggesting that the monzonite porphyries underwent higher degrees of partial melting, but from a common source. Consequently, the Habo porphyries were most likely generated by different degrees of partial melting of the lower crust source, as evidenced by the electron probe analysis of the inclusion and the suite of host rock minerals found in the contemporaneous Liuhe Alkali-rich Porphyries in western Yunnan, which show that the magma source depth should be the bottom of the lower crust (Zhang, 2017).

As shown in Fig. 10a，the Rb/Sr=0.38–0.45 and Ba/Rb=2.93–4.53, suggests the nnature of melt produced from phlogopite-bearing mantle sources. In addition, these values are similar in this respect to the potassic rocks of

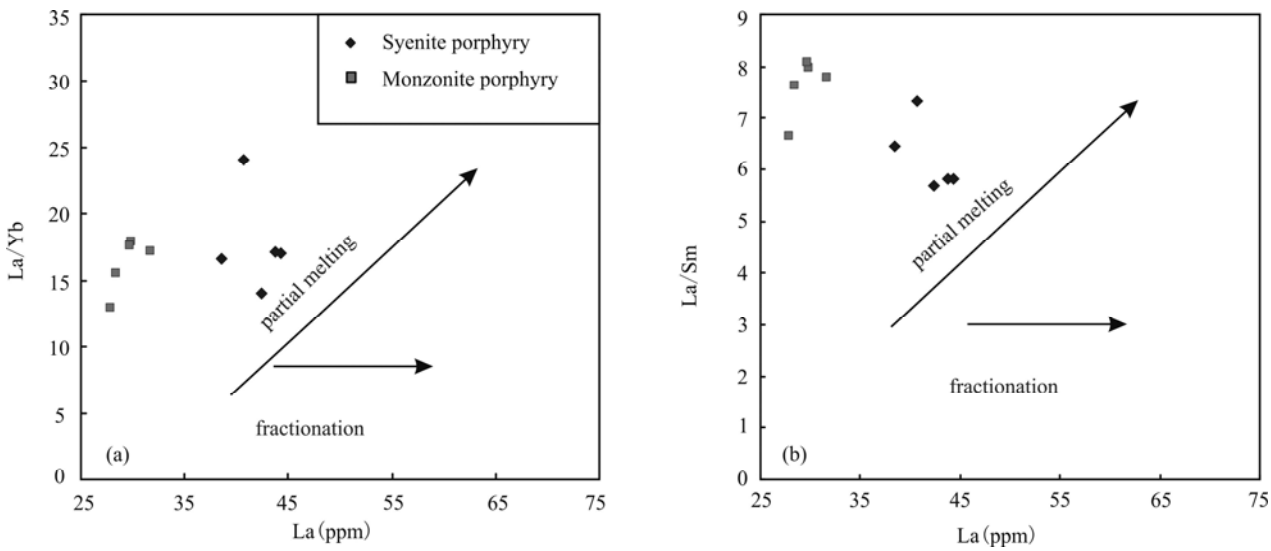


Fig. 9. (a) La/Yb vs La and (b) La/Sm vs La diagram for syenite porphyries and monzonite porphyries from Habo.

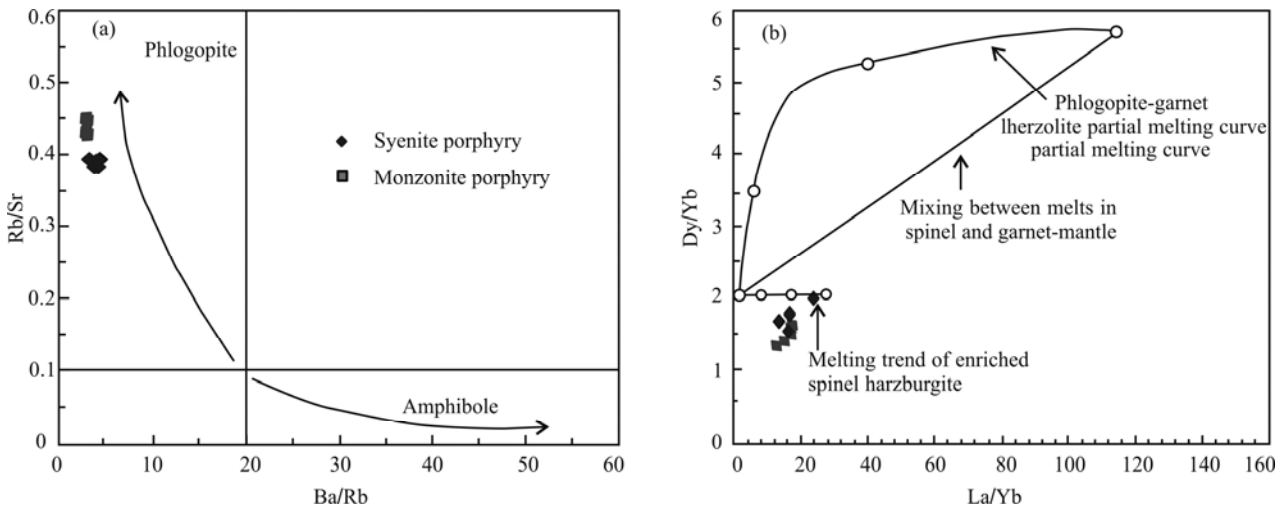


Fig. 10. (a) Rb/Sr vs. Ba/Rb and (b) La/Yb vs. Dy/Yb (melting curves are after Xu et al., 2001).

SE Tibet and elsewhere in the Ailaoshan–Red River shear zone (Fig. 10b) which were generated as small melt fractions from a mica-bearing spinel harzburgitic lithospheric mantle (Xu et al., 2001). Therefore, the Habo porphyries are related to common post-collisional processes, with the source region most likely derived from a phlogopite-bearing lithospheric mantle that had already been modified by subduction- related processes (Pearce, 1983).

### 5.3 Implications for geodynamic evolution and tectonic significance

The Ailaoshan tectonic belt, located in the southeast margin of the Tibetan plateau, is the most important boundary structure on the Yangtze and Simao blocks and plays an important role in the process of the southeastward movement of the Indosinian plate and the post-collisional extension in eastern Tibet. In this paper, isotope chronology is limited to 35.2–37.5 Ma, which coincides with the late-collisional transform structural stage of plate movement (Hou and Cook, 2009). In the Rb vs. (Y+Nb) and Nb vs. Y tectonic discrimination diagrams (Pearce et al., 1984), all the porphyry samples plot within the syn-collision granites field (Fig. 11), indicating that the Habo porphyries were formed in a collisional tectonic setting. In this stage, there are a series of regional thrust, nappe and strike-slip faults (Deng et al., 2014a). The strike-slip and shearing movement is the genesis of partial melting in the magma source region. The depth of the shearing movement has a direct effect on the magma source region. Based on the above discussions, it is proposed that the Habo porphyries are from a mica-bearing spinel harzburgitic lithospheric mantle located at 75–85 km of depth (Mckenzie and O′ Nions, 1991). Partial melting of the enriched mantle materials is caused by the strike-slip shearing action and mafic magma is produced. The underplating of magma induces the anatexis of lower crust material, forming the felsic magma. At the same time, strike-slip shear movement with a pull-apart effect provides space for the rise of magma and channels, and fractional crystallization in the process of the original magma rising induced the alkaline rock from basic to acid emplacement in a relatively short time.

## 6 Conclusions

(1) LA-MC-ICP-MS U–Pb dating of zircons from the syenite porphyry and monzonite porphyry in the Habo polymetallic ore field constrains the emplacement of the porphyries to a period ranging from 34.54 ±0.63 to 35.25 ±0.51 Ma, which coincides with the ages of potassic intrusive rocks within the Jinshajiang–Ailaoshan magmatic belt.

(2) The Habo syenite porphyry and monzonite porphyry have similar geochemistry and sources. It is interpreted that these porphyries were most likely sourced from a spinel lherzolite that included minor amount of phlogopite.

(3) It is proposed that the Habo porphyries were derived from partial melting of a felsic source in the thickened lower crust mixing with the mantle-derived mafic magma.

## Acknowledgments

We are grateful to the anonymous reviewers for their significant and constructive comments. The work was financially supported by the National Natural Science Foundation of China (41372208 and 41776056) and Natural Science Foundation of Guangdong Province (2017A030310395). Prof. Zhang Yuquan is thanked for his

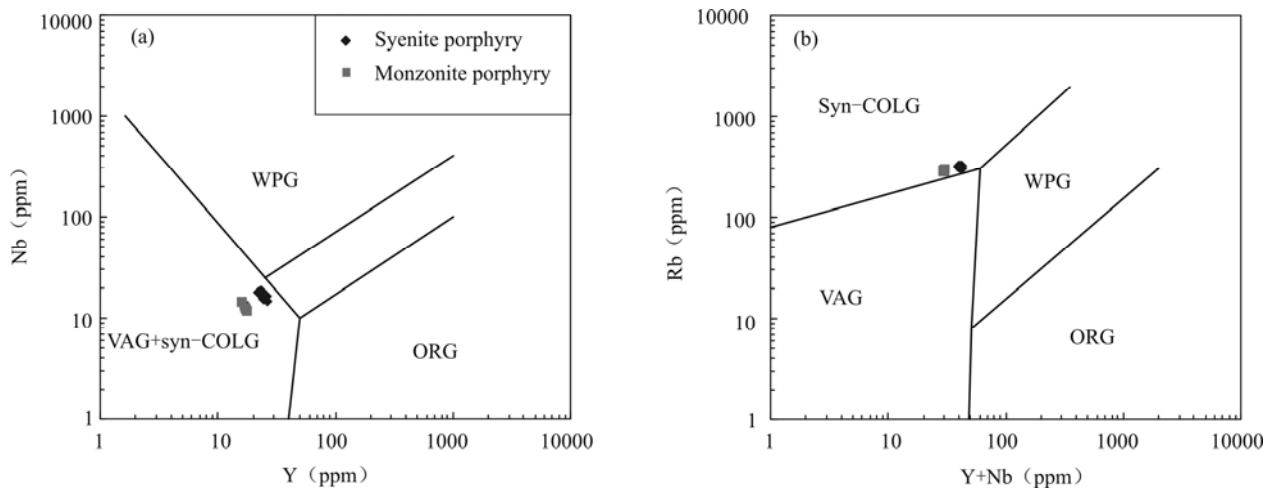


Fig. 11. Tectonic discrimination diagrams for the Habo porphyries.
(a), Y vs. Nb (after Pearce et al., 1984); (b), (Y+Nb) vs. Rb plot (after Harris et al., 1986).

help in the discussion and polishing of this manuscript. We thank Prof. Tu Xianglin for the help with the chronology calculations, and Profs. Sun Weidong, and Liu Yin for the geochemical analysis.

Manuscript received Dec. 14, 2017
accepted Mar. 15, 2018
edited by Fei Hongcai

## References

Barry, T.L., Pearce, J.A., Leat, P.T., Millar, I.L., and Roex, A.P.L., 2006. Hf isotope evidence for selective mobility of high-field-strength elements in a subduction setting: South Sandwich Islands. *Earth & Planetary Science Letters*, 252: 223–244.

Bi Xianwu, Hu Ruizhong, Peng Jiantang, Wu Kaixin, Su Wenchao and Zhan Xinzhi, 2005. Geochemical characteristics of the Yao'an and Machangqing alkaline-rich intrusions. *Acta Petrologica Sinica*, 21: 113–124 (in Chinese with English abstract)

Black, L.P., Kamo, S.L., Williams, I.S., Mundil, R., Davis, D.W., Korsch, R.J., and Foudoulis, C., 2003. The application of SHRIMP to Phanerozoic geochronology; a critical appraisal of four zircon standards. *Chemical Geology*, 200: 171–188.

Bolhar, R., Weaver, S. D., Whitehouse, M. J., Palin, J. M., Woodhead, J. D., and Cole, J.W., 2008. Sources and evolution of arc magmas inferred from coupled o and Hf isotope systematics of plutonic zircons from the cretaceous separation point suite (New Zealand). *Earth & Planetary Science Letters*, 268: 312–324.

Bui, H.B., Ngo, X.T., Song, Y., Itaya, T., Yagi, K., Khuong T.H., and Nguyen, T.D., 2016. K-Ar dating of fault gouges form the Red River fault zone of Vietnam. *Acta Geologica Sinica* (English Edition), 90(5): 1653–1663.

Chappell, B.W., and White, A.J.R., 1992. I- and S-type granites in the Lachlan Fold Belt. *Transactions of the Royal Society of Edinburgh Earth Sciences*, 83: 1–26

Chen Jianlin, Xu Jifeng, Wang Baodi, Kang Zhiqiang and Li Jie, 2010. Origin of Cenozoic alkaline potassic volcanic rocks at KonglongXiang, Lhasa terrane, Tibetan Plateau: Products of partial melting of a mafic lower-crustal source? *Chemical Geology*, 273: 286–299.

Cheng Yanbo and Mao Jingwen, 2010. Age and geochemistry of granites in Gejiu area, Yunnan province, SW China: constraints on their petrogenesis and tectonic setting. *Lithos*, 120: 258–276

Chung Sunlin; Lee Tungyi, Lo Chinghua, Wang Peiling, Chen Chinyu, Trong Yem, N., Trong Hoa, T., and Wu Genyao, 1997. Intraplate extension prior to continental extrusion along the Ailao shan-Red River shear zone. *Geology*, 25: 311–314

Crofu, F, Hanchar, J.M., Hoskin, P.W.O., and Kinny, P., 2003. Atlas of zircon textures. *Reviews in Mineralogy and Geochemistry*, 53: 469–495

Deng Junliang, Wang Changming and Li Gongjian, 2012. Style and process of the superimposed mineralization in the Sanjiang Tethys. *Acta Petrologica Sinica*, 28: 1349–1361 (in Chinese with English abstract)

Deng Junliang, Wang Qingfei, Li Gongjian and Santosh, M., 2014. Cenozoic tectono-magmatic and metallogenic processes in the Sanjiang region, southwestern China. *Earth-Science Reviews*, 138: 268–299

Deng Junliang, Wang Qingfei, Li Gongjian and Santosh, M., 2014b. Cenozoic tectono-magmatic and metallogenic processes in the Sanjiang region, Southwestern China. *Earth-Science Reviews*, 138: 268–299

Deng Junliang, Wang Qingfei, Li Gongjian, Hou Zengqian, Jiang Chengzhu and Danyushevsky, L., 2015. Geology and genesis of the giant Beiya porphyry-skarn gold deposit, northwestern Yangtze Block, China. *Ore Geology Reviews*, 70: 457–485

Deng Junliang, Wang Qingfei, Li Gongjian, Li Chusi and Wang Changming, 2014a. Tethys tectonic evolution and its bearing on the distribution of important mineral deposits in the sanjiang region, SW China. *Gondwana Research, 26*: 419–437.

Deng Junliang, Yang Liqiang and Wang Changming, 2011. Research advances of superimposed orogenesis and metallogenesis in the Sanjiang Tethys. *Acta Petrologica Sinica*, 27: 2501–2509 (in Chinese with English abstract)

Deng Wanming, Huang Xuan and Zhong Dalai., 1998. Petrological characteristics and genesis of Cenozoic alkali-rich porphyry in west Yunnan, China. *Scientia Geologica Sinica*, 33: 412–425 (in Chinese with English abstract)

Fu Yu, Sun Xiaomin, Lin Hai, Zhou Haoyang, Li Xin, Ouyang Xianqing, Jiang Liyi, Shi Guiyong and Liang Yeheng, 2015. Geochronology of the giant Beiya gold-polymetallic deposit in Yunnan Province, Southwest China and its relationship with the petrogenesis of alkaline porphyry. *Ore Geology Reviews*, 71: 138–149

He Wenyan, Mo Xuanxue, He Zhonghua, White, N.C., Chen Jinbiao, Yang Kaihui, Wang Rui, Yu Xuehui, Dong Guo chen and Huang Xiongfei, 2015. The geology and mineralogy of the beiya skarn gold deposit in Yunnan, southwest China. *Economic Geology*, 110: 1625–1641

He Wenyan, Mo Xuanxue, Yang Liqiang, Xing Yanlu, Dong Guochen, Yang Zhen, Gao Xue, Bao Xinsheng, 2016. Origin of the Eocene porphyries and mafic microgranular enclaves from the Beiya porphyry Au polymetallic deposit, western Yunnan, China: implications for magma mixing/mingling and mineralization. *Gondwana Research*, 40: 230–248

He Wenyan, Mo Xuanxue, Yu Xuehui, Dong Guochen, He Zhonghua, Huang Xiongfei, Li Xiaowei and Jiang Lili, 2014. Genesis and geodynamic settings of lamprophyres from Beiya, western Yunnan: Constraints from geochemistry, geochronology and Sr-Nd-Pb-Hf isotopes. *Acta Petrologica Sinica*, 30: 3287–3300 (in Chinese with English abstract)

He Wenyan, Mo Xuanxue, Yu Xuehui, He Zhonghua, Dong Guochen, Liu Xiaobo, Su Gangsheng and Huang Xiongfei, 2013. Zircon U-Pb and molybdenite Re-Os dating for the Beiya gold – polymetallic deposit in the western Yunnan Province and its geological significance. *Acta Petrologica Sinica*, 29: 1301–1310 (in Chinese with English abstract)

Hou Zengqian, Ma Hongwen, Khin, Z., Zhang Yuquan, Wang Mingjie, Wang Zeng, Pan Guitang and Tang Renli, 2003. The Himalayan Yulong porphyry copper belt: produced by large-scale strike-slip faulting at Eastern Tibet. *Economic Geology*, 98: 125–145

Hou Zengqian, Mo Xuanxue, Zhu Qinwen and Shen Shangyue, 1996. Mantle plume in the Sanjiang Paleo-Tethyan lithosphere: evidence from mid-ocean ridge basalts. *Acta Geoscientica Sinica*, 17: 362–375 (in Chinese with English abstract)

Hou Zengqian, Zaw, K., Pan Guitang, Mo Xuanxue, Xu Qiang, Hu Yunzhong and Li Xingzhen, 2007. Sanjiang Tethyan metallogenesis in S.W. China: Tectonic setting, metallogenic epochs and deposit types. *Ore Geology Reviews*, 31: 48–87

Hu Xiangzhao and Huang Zhen 1997. The petrology and petrogensis of the Yangtze plantfrom western margins alkali-rich granite porphyry. *Geotectonica et Metallogenia*, 21: 173–180 (in Chinese with English abstract)

Jiang Xiaojun, Yan Qinggao, Li Wenchang, Li Chao, Wu Peng, Guan Shenjin, Yu Haijun and Li Jinlong, 2018. The metallogenic age and geodynamic setting of the Laojiezi Pb-Ag polymetallic deposit, central Yunnan Province: Evidence from Re Os isotope of sulfides. *Acta Geologica Sinica,* 92: 1280–1296 (in Chinese with English abstract)

Le Maitre, R.W., Streckeisen, A., Zanettin, B., Le Bas, M.J., Bonin, B., Bateman, P., Bellieni, G., Dudek, A., Efremova, S.A., Keller, J., Lameyre, J., Sabine, P.A., Schmid, R., Søensen, H., and Woolley, A.R., 2002. *Igneous Rocks: A Classification Glossary of Terms*. Cambridge: Cambridge University Press, 236.

Liang HuaYing, Mo Jihai, Sun Weidong, Yu Hengxiang, Zhang Yuquan and Allen, C.M., 2008. Study on the duration of the ore-forming system of the Yulong giant porphyry copper deposit in eastern Tibet, China. *Acta Petrologica Sinica*, 24: 2352–2358(in Chinese with English abstract)

Liu Bo, Liu Huan, Zhang Changqing, MaoZhihao, Zhou Yunman, Huang Hua, He Zhonghua and Su Gangsheng, 2015. Geochemistry and geochronology of porphyries from the Beiya gold–polymetallic orefield, western Yunnan, China. *Ore Geology Reviews*, 69: 360–379.

Liu Yongsheng, Gao Shan, Hu Zhaochu, Gao Changgui, Zong Keqing and Wang Dongbing, 2010. Continental and oceanic crust recycling-induced melt-peridotite interactions in the trans-north China orogen: U-Pb dating, Hf isotopes and trace elements in zircons from mantle xenoliths. *Journal of Petrology*, 51: 537–571.

Liu Yongsheng, Hu Zhaochu, Gao Shan, Gunther, D., Xu Juan, Gao Changgui and Chen Haihong, 2008. In situ analysis of major and trace elements of anhydrous minerals by LA-ICP-MS without applying an internal standard. *Chemical Geology*, 257: 34–43.

Lu Yongjun, Kerrich, R., Cawood, P.A., McCuaig, T.C., Hart, C.J.R., Li Zhengxiang, Hou Zengqian and Bagas, L., 2012. Zircon SHRIMP U–Pb geochronology of potassic felsic intrusions in western Yunnan, SW China: constraints on the relationship of magmatism to the Jinsha suture. *Gondwana Research*, 22: 737–747.

Ludwing, K., 2003. User's manual for Isoplot 3.00: A geochronological toolkit for Microsoft Excel. *Special Publication, Berkeley Geochronology Center*, 1–70.

Maniar, P.D., and Piccoli, P.M., 1989. Tectonic discrimination of granitoids. *Bulletin of the Geological Society of America*, 101: 635–643.

Mckenzie, D., and O′Nions, R.K., 1991. Partial melt distributions from inversion of rare earth element concentrations. *Journal of Petrology*, 32: 1021–1091

Metcalfe, I., 2006. Palaeozoic and Mesozoic tectonic evolution and palaeogeography of East Asian crustal fragments: The Korean Peninsula in context. *Gondwana Research*, 9: 24–46

Metcalfe, I., 2013. Gondwana dispersion and Asian accretion: Tectonic and palaeogeographic evolution of eastern Tethys. *Journal of Asian Earth Sciences*, 66: 1–33

Middlemost, E.A.K., 1994. Naming materials in the magma igneous rock system. *Earth-Science Reviews*, 37: 215–224.

Tapponnier, P., Lacassin, P., Leloup, R., Schärer, P.H., U., Zhong Dalai, Wu Haiwei, Liu Xiaohan, Ji Shaocheng, Zhang Lianshang and Zhong Jiayou, 1990. The Ailao Shan-Red River metamorphic belt: Tertiary left-lateral shear between Indochina and South China. *Nature*, 343: 431–437

Pearce, J.A., Harris, N.B.W., and Tindle, A.G., 1984. Trace element discrimination diagrams for the tectonic interpretation of granitic rocks. *Journal of Petrology*, 25: 956–983

Pearce, N.J.G., Perkins, W.T., Westgate, J.A., Gorton, M.P., Jackson, S.E., Neal, C.R., and Chenery, S.P., 1997. A compilation of new and published major and trace element data for NIST SRM 610 and NIST SRM 612 glass reference materials. *Geostandard Newsletter*, 21: 115–144.

Richards, J.P., 2009. Post-subduction porphyry cu-au and epithermal au deposits: products of remelting of subduction-modified lithosphere. *Geology*, 37: 247–250

Rickwood, P.C., 1989. Boundary lines within petrologic diagrams which use oxides of major and minor elements. *Lithos*, 22: 247–263.

Streckeisen, A., and Le Maitre, R.W., 1979. A chemical approximation to the modal QAPF classification of the igneous rocks. Neues Jahrbuch fur Mineralogie, Abhandlungen 136: 169–206.

Sun, S.S., and McDonough, W.F., 1989. Chemical and isotopic systematics of oceanic of oceanic basalts: implications for mantle composition and processes. In: Saunders, A.D., and Norry, M.J. (eds.), *Magmatism in the Ocean Basins*. Geological Society of London, Special Publications, 42: 313–345.

Tran, M.D., Liu Junlai, Nguyen, Q.L., Chen Yue, Tang Yuan, Song Zhijie, Zhang Zhaochong and Zhao Zhidan, 2014. Cenozoic high-K alkaline magmatism and associated Cu-Mo-Au mineralization in the Jinping-Fan Si Pan region, southeastern Ailao Shan-Red River shear zone, southwestern China-northwestern Vietnam. *Journal of Asian Earth Sciences*, 79: 858–872

Tu Xianglin, Zhang Hong, Deng Wenfeng, Ling Mingxing, Liang Huaying, Liu Ying and Sun Wei-dong, 2011. Application of Resolution in-situ laser ablation ICP-MS in trace element analyses. *Geochimica*, 40: 83–98 (in Chinese with English abstract).

Turner, S., Arnaud, N., Liu, J.Q, Rogers, H.C., Harris, N, Kellty, S, Vancalsteren, P., and Deng Wanming, 1996. Post-collision, shoshonitic volcanism on the Tibetan plateau: implications for convective thinning of the lithosphere and the source of ocean island basalts. *Journal of Petrology*, 37: 45–71

Wang Denghong, Qu Wenjun, Li Zhiwei, Yin Hanlong and Chen Yuchuan, 2005. Mineralization episode of porphyry copper deposits in the Jinshajiang - Red River mineralization belt: Re -Os dating. *Science in China Series D-Earth Science*, 48: 192–198

Wang Jianghai, Yin, A., Harrison, T. M., Grove, M., Zhang Yuquan and Xie Guanghong, 2001. A tectonic model for Cenozoic igneous activities in the eastern Indo–Asian collision zone. *Earth & Planetary Science Letters,* 188: 123–133.

Wang Qingfei, Deng Jun, Li Chusi, Li Gongjian, Yu Li and Qiao Long, 2014a. The boundary between the Simao and Yangtze

blocks and their locations in Gondwana and Rodinia: constraints from detrital and inherited zircons. *Gondwana Research*, 26: 438–448

Wang Yinhong, Xue Chunji, Liu Jiajun, Wang Jianping, Yang Juntao, Zhang Fangfang, Zhao Zenan, Zhao Yunjiang and Liu Bin., 2015. Early Carboniferous adakitic rocks in the area of the Tuwu deposit, eastern Tianshan, NW China: slab melting and implications for porphyry copper mineralization. *Journal of Asian Earth Sciences, 103*: 332–349.

White, N.C., Yang, Kaikui and Li Wenchang, 2007. Discovery of the Habo porphyry Cu–Au–(Mo) system in Southern China: its lessons for exploration everywhere. In: Andrew, C.J., et al. (eds.), *Digging Deeper: Proceedings of the 9th Biennial SGA Meeting*, Dublin, Irish Association for Economic Geology, Dublin, Ireland, 1: 489–492.

Woodhead, J, Hergt, J., Shelley, M., Eggins, S., and Kemp, R., 2004. Zircon Hf-isotope analysis with an excimer laser, depth profiling, ablation of complex geonmetries and concomitant age estimation. *Chemical Geology*, 209: 121–135.

Wu YuanBao and Zheng Yongfei, 2004. Genesis of zircon and its constraints on interpretation of U-Pb age. *Chinese Science Bulletin*, 49: 1554–1569

Xia Ping and Xu Yigang, 2004. Domains and enrichment mechanism of the lithospheric mantle in western Yunnan: a comparative study on two types of Cenozoic ultrapotassic rocks. *Science in China Series D*, 48: 326–337.

Xu Leiluo, Bi Xianwu, Hu Ruizhong, Zhang Xingchun, Su Wenchao, Qu Wenjun, Hu Zhaochu and Tang Yongyong, 2012. Relationships between porphyry Cu-Mo mineralization in the Jinshajiang-Red River metallogenic belt and tectonic activity: Constraints from zircon U-Pb and molybdenite Re-Os geochronology. *Ore Geology Reviews*, 48: 460–473

Yan Qinggao, Jiang Xiaojun, Wu Peng, Sun Huiyi and Guan Shenjin, 2017. Zircon SHRIMP U-Pb geochronology and volcanic edifice division of the Laojiezi intraplate alkali-rich volcanic rocks in Yao'an, central Yunnan Province. *Acta Geologica Sinica,* 91: 1743–1759 (in Chinese with English abstract)

Yang Liqiang, Liu Jiangtao, Zhang Chuang, Wang Qingfei, Ge Liangsheng and Wang ZhongLiang. ,2010. Superimposed orogenesis and metallogenesis: an example from the orogenic gold deposits in Ailaoshan gold belt, Southwest China. *Acta Petrologica Sinica*, *26*: 1723–1739.

Yang Zhen, Yang Liqiang, He Wenyan, Gao Xue, Liu Xudong, Bao Xinshang and Lu Yiguan, 2017. Control of magmatic oxidation state in intracontinental porphyry mineralization: a case from cu (Mo–Au) deposits in the Jinshajiang–Red River metallogenic belt, SW China. *Ore Geology Reviews*, 90:827-846.

Yin, A., and Harrison, T.M., 2000. Geologic evolution of the Himalayan-Tibetan orogen. *Annual Review of Earth & Planetary Sciences*, *28*: 211–280.

Yogodzinski, G.M., Vervoort, J.D., Brown, S.T.= and Gerseny, M., 2010. Subduction controls of hf and nd isotopes in lavas of the aleutian island arc. *Earth & Planetary Science Letters*, 300: 226–238.

Yuan Honglin, Gao Shan, Liu Xiaoming, Li Huiming, Günther, D., and Wu Fuyuan, 2010. Accurate U‐Pb age and trace element determinations of zircon by laser ablation‐inductively coupled plasma‐mass spectrometry. *Geostandards & Geoanalytical Research, 28*: 353–370.

Zhang Jing, Deng Jun, Li Shihui, Yan Ni, Yang Liqiang, Ma Nan, Wang Qingfei and Gong QingJie, 2010.Petrological characteristics of magmatites and their relationship with gold mineralization in the Chang'an Gold Deposit in southern Ailaoshan metallogenic belt. *Acta Petrologica Sinica*, 26: 1740–1750

Zhang Yuquan and Xie Yingwen, 1997. Geochronology and Nd, Sr isotopic features of alkalic-rich intrusive rocks along the Ailao Shan-Jinshajiang belt. *Science in China Series D-Earth Science*, 27: 289–293

Zhang Yuquan, Xie Yingwen and Tu Guangzhi, 1987. Preliminary studies of the alkali-rich intrusive rocks in the Ailaoshan-Jinshajiang belt and their bearing on rift tectonics. *Acta Petrologica Sinica*, 1: 17–26 (in Chinese with English abstract)

Zhang Yong, 2017. Geochronology and geochemistry of alkali-rich porphyries and its xenoliths in Liuhe and Xiaoqiaotou, Western Yunnan. China University of Geosciences (Beijing), Beijing, China, 69 (in Chinese with English abstract)

Zhu Dicheng, Mo Xuexuan, Wang Liquan, Zhao Zhidan, Niu Yaoling, Zhou Changyong and Yang Yueheng, 2009. Petrogenesis of highly fractionated I-type granites in the Zayu area of eastern Gangdese, Tibet: constraints from zircon U–Pb geochronology, geochemistry and Sr–Nd–Hf isotopes. *Science in China Series D*, 52: 1223–1239

Zhu Xiangping, Mo Xuanxue, White, N.C., Zhang Bo, Sun Mingxiang, Wang Shuxian, Zhao Sili and Yang Yong, 2013. Petrogenesis and metallogenic setting of the Habo porphyry Cu-(Mo-Au) deposit, Yunnan, China. *Journal of Asian Earth Sciences*, 66: 188–203

## About the first author

XIA Bin, male, born in 1959, Ph.D. He is now a professor at School of Marine Sciences, Sun Yat-sen University, and is mainly engaged in structural geology and petroleum geology researches. E-mail: xiabin@mail.sysu.edu.cn.